Intrinsic timing, not temporal prediction, underlies ramping dynamics in visual and parietal cortex during passive behavior

Yicong Huang[1], Ali Shamsnia[2], Mengze Chen [2], Shuang Wu[2], Timothy Stamm[2], Sophie Medico[2], Farzaneh Najafi[2#]

[1] Wallace H Coulter Department of Biomedical Engineering, Georgia Institute of Technology and Emory University

[2] School of Biological Sciences, Georgia Institute of Technology

Corresponding author: fnajafi3@gatech.edu

Graphical Abstract

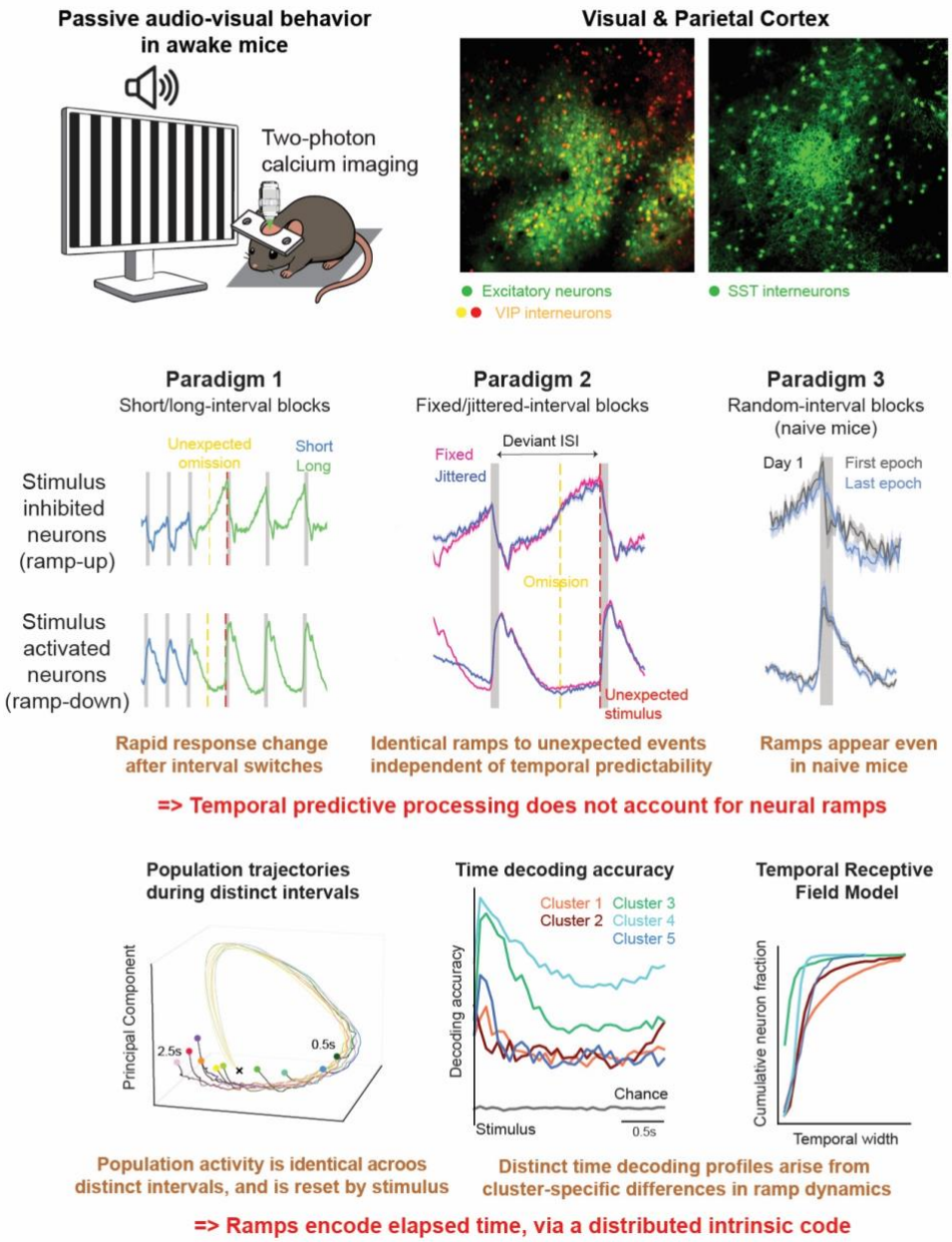

Abstract

Neural activity following regular sensory events can reflect either the elapsed time since the previous event (*temporal signaling*) or temporal predictions and prediction errors about the next event (*temporal predictive processing*). These mechanisms are often confounded, yet dissociating them is essential for understanding neural circuit computations.

We addressed this by performing two-photon calcium imaging from distinct cell types (excitatory, VIP, and SST) in layer 2/3 of the medial visual cortex (VIS) and the posterior parietal cortex (PPC) while awake mice passively viewed audio-visual stimuli under temporal contexts with different inter-stimulus interval (ISI) distributions. Computational modeling revealed distinct functional clusters of neurons, stimulus-activated (ramp-down) and stimulus-inhibited (ramp-up), with characteristic kinetics and area- and cell-type-specific biases.

Importantly, all functional clusters were invariant to temporal predictability, shifted immediately when temporal statistics changed, and existed even in naïve mice—findings *inconsistent* with predictions from temporal predictive processing frameworks. Elapsed-interval information could nonetheless be decoded, and heterogeneous kinetics underlay how well each cluster represented interval duration, leading to a distributed, learning-independent population code for time.

These results demonstrate that activity in VIS and PPC arises from stimulus-evoked dynamics whose intrinsic evolution encodes elapsed time, rather than from temporal predictive processing, redefining the mechanistic origin of ramping and omission-related activity in visual and parietal cortices. We propose that temporal predictive processing may instead be implemented in other circuits or recruited in VIS/PPC during task-engaged behavior.

Introduction

The brain continuously encodes the passage of time and generates expectations about when future events will occur. These temporal computations are critical for perception, motor control, and learning, yet their neural underpinnings remain debated (Nobre et al., 2007).

Neural activity between sensory events may reflect two distinct processes: elapsed-time signaling, which encodes the duration since the previous event, and temporal predictive processing, which represents the expected timing of the next event. These processes unfold concurrently; hence, it is often difficult to determine whether neural responses in a given circuit reflect temporal tracking or predictive processing mechanisms.

Temporal signaling, the encoding of elapsed time, is achieved through multiple mechanisms (Coull et al., 2011; Tsao et al., 2022), such as ramping (gradual changes in neural activity) (Cueva et al., 2020; De Corte et al., 2022; Narayanan, 2016), sequential activation of neurons (S. Zhou et al., 2020), and population trajectories, where activity patterns of recurrently-connected neurons evolve through a high-dimensional state space, with each state carrying information about elapsed time (Machens et al., 2010; Mante et al., 2013; Murray et al., 2014; Paton & Buonomano, 2018; Wang et al., 2018).

Synaptic mechanisms, such as short-term plasticity that modulate how neurons respond to inputs over time (Feldman, 2012; Laje & Buonomano, 2013), together with variability in intrinsic time constants, generate heterogeneous dynamics across the population. This diversity acts as a temporal basis set: overlapping dynamics tile different segments of an interval, allowing downstream circuits to reconstruct elapsed time from distributed activity. Such population-level coding has been observed across cortical, striatal, hippocampal, and cerebellar circuits (Bernacchia et al., 2011; Buonomano & Maass, 2009; Chabrol et al., 2015; Garcia-Garcia et al., 2024; Herzfeld & Lisberger, 2025; MacDonald et al., 2011; Matell et al., 2003; Medina & Mauk, 2000; Mello et al., 2015; Pastalkova et al., 2008).

In the cortex, both sensory and associative areas demonstrate temporal processing. For example, neurons in the posterior parietal cortex (PPC) contribute to interval production and categorization (Bueti & Walsh, 2009; Hayashi et al., 2015; Janssen & Shadlen, 2005; Leon & Shadlen, 2003; Schneider & Ghose, 2012), and neurons in frontal/prefrontal cortices demonstrate population trajectories that flexibly “scale” with the demanded interval length (Kim et al., 2013; Wang et al., 2018; Xu et al., 2014). Primary sensory cortices also show timing signatures when stimuli are predictable: neurons in primary visual and auditory cortex “remember” recent intervals, through stimulus-evoked state shifts that depend on short-term depression/facilitation (Gavornik & Bear, 2014; Jaramillo & Zador, 2011; Yu et al., 2022).

Predictive processing, on the other hand, suggests that cortical areas contain internal models of the world, which generate predictions that are compared with sensory inputs. When a mismatch occurs, prediction error (PE) signals are generated to update the internal model (Aizenbud et al., 2025; Friston & Kiebel, 2009; Keller & Mrsic-Flogel, 2018; Rao & Ballard, 1999). This canonical computation has been identified across many brain regions and species, and applies to both the identity and the timing of sensory inputs—that is, *what* and *when* a stimulus will occur (Aizenbud et al., 2025). Multiple cortical areas—including visual and parietal cortex—have been implicated in predictive processing (Aizenbud et al., 2025; Fiser et al., 2016; Furutachi et al., 2024; Garrett, Groblewski, Piet, Ollerenshaw, Najafi, et al., 2023; Garrett et al., 2020; Hamm et al., 2021; Najafi et al., 2025; Van Derveer et al., 2023; Z. C. Zhou et al., 2020).

Cell-type-specific studies demonstrate a key role for inhibitory neurons—particularly VIP and SST interneurons—in predictive processing (VIP: vasoactive intestinal peptide; SST: somatostatin). VIP neurons in primary and higher visual areas respond to the change (G. Bastos et al., 2023; Furutachi et al., 2024) or omission (Furutachi et al., 2024; Garrett, Groblewski, Piet, Ollerenshaw, Yavorska, et al., 2023; Garrett et al., 2020; Knudstrup et al., 2025; Najafi et al., 2025; Nitzan & Buzsáki, 2025) of expected visual stimuli. SST interneurons, in the PPC, include a molecularly defined subset that carries an error-correction signal during navigation tasks (Green et al., 2023). Computational modelling and circuit dissection suggest that VIP–SST–Excitatory disinhibitory circuit can give rise to prediction-error neurons (Hertäg & Sprekeler, 2020; Keller et al., 2020).

Figure 1

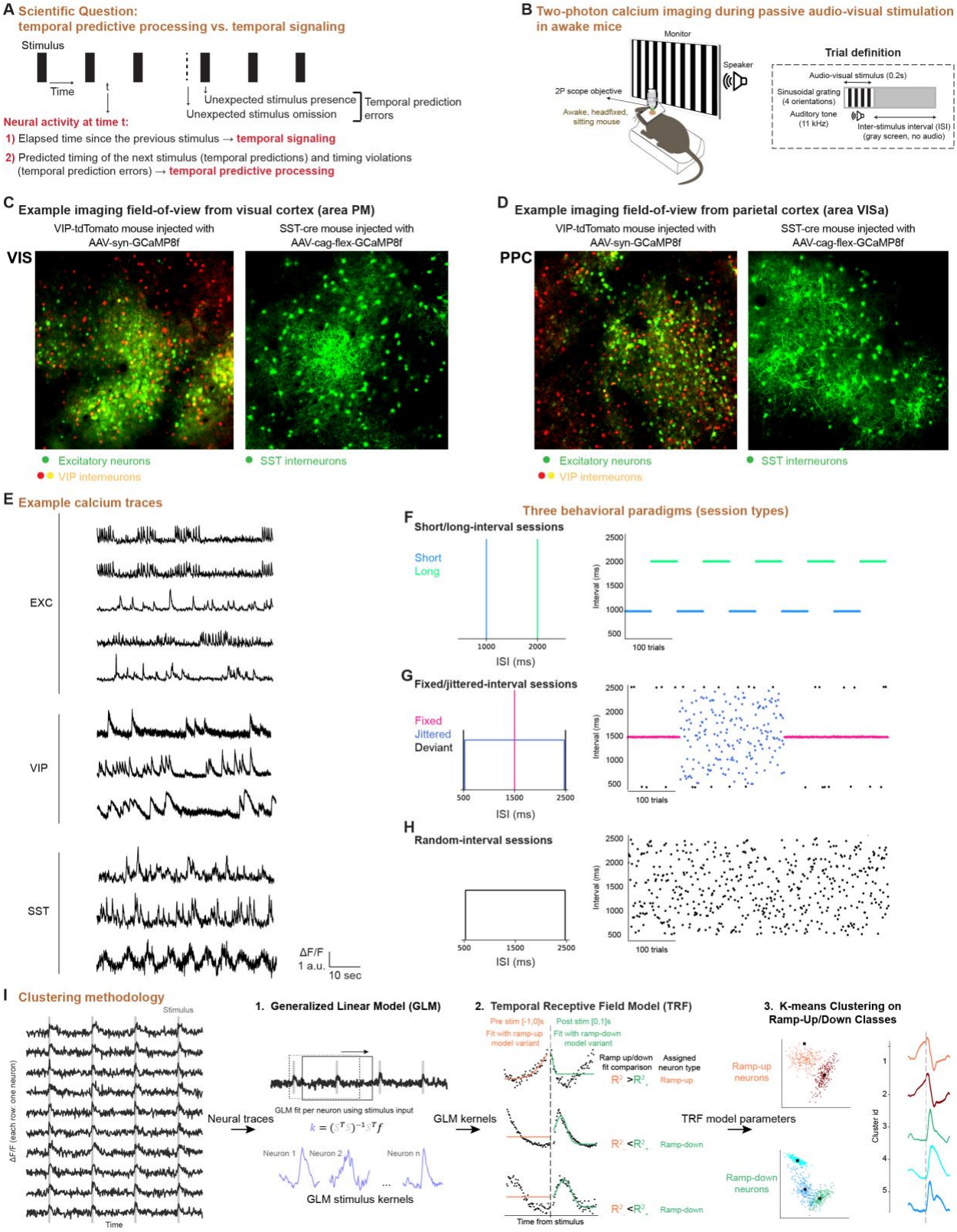
A Scientific Question:
temporal predictive processing vs. temporal signaling
Stimulus
Time
t
Unexpected stimulus presence
Unexpected stimulus omission
Temporal prediction errors
Neural activity at time t:
1) Elapsed time since the previous stimulus → temporal signaling
2) Predicted timing of the next stimulus (temporal predictions) and timing violations (temporal prediction errors) → temporal predictive processing
B Two-photon calcium imaging during passive audio-visual stimulation in awake mice
Monitor
Speaker
2P scope objective
Awake, headfixed, sitting mouse
Trial definition
Audio-visual stimulus (0.2s)
Sinusoidal grating (4 orientations)
Auditory tone (11 kHz)
Inter-stimulus interval (ISI) (gray screen, no audio)
C Example imaging field-of-view from visual cortex (area PM)
VIP-tdTomato mouse injected with AAV-syn-GCaMP8f
SST-cre mouse injected with AAV-cag-flex-GCaMP8f
VIS
Excitatory neurons
VIP interneurons
SST interneurons
D Example imaging field-of-view from parietal cortex (area VISa)
VIP-tdTomato mouse injected with AAV-syn-GCaMP8f
SST-cre mouse injected with AAV-cag-flex-GCaMP8f
PPC
Excitatory neurons
VIP interneurons
SST interneurons
E Example calcium traces
EXC
VIP
SST
ΔF/F
1 a.u.
10 sec
Three behavioral paradigms (session types)
F Short/long-interval sessions
Short
Long
ISI (ms)
Interval (ms)
100 trials
G Fixed/jittered-interval sessions
Fixed
Jittered
Deviant
ISI (ms)
Interval (ms)
100 trials
H Random-interval sessions
ISI (ms)
Interval (ms)
100 trials
I Clustering methodology
Stimulus
ΔF/F (each row: one neuron)
Time
Neural traces
1. Generalized Linear Model (GLM)
GLM fit per neuron using stimulus input
$k = (\Delta^T \Delta)^{-1} \Delta^T f$
Neuron 1
Neuron 2
Neuron n
GLM stimulus kernels
GLM kernels
2. Temporal Receptive Field Model (TRF)
Pre stim [-1,0]s
Fit with ramp-up model variant
Post stim [0,1]s
Fit with ramp-down model variant
Ramp up/down fit comparison
Assigned neuron type
Ramp-up
Ramp-down
Time from stimulus
TRF model parameters
3. K-means Clustering on Ramp-Up/Down Classes
Ramp-up neurons
Ramp-down neurons
Cluster id

Figure 1. Experimental design to disentangle temporal signaling from temporal predictive processing.

A) Neural activity at each timepoint could reflect one of the 2 processes: **(1)** temporal signaling, i.e., encoding elapsed time since the previous stimulus; or **(2)** Temporal predictive processing, i.e., generating predictions and prediction errors about the timing of the upcoming stimulus. Temporal prediction errors occur when a stimulus is presented earlier or later ('omission') than expected.

B) Left: Awake, head-fixed mice received repeating audio-visual stimuli (0.2s), separated by an inter-stimulus interval (ISI; gray screen), while two-photon calcium imaging was performed from the medial visual cortex (area PM) and posterior parietal cortex (PPC, area VISa). **Right:** A trial is defined as a 200ms audio-visual stimulus followed by an ISI with a gray screen and no auditory tone. ISI duration varied across paradigms (see F-H).

C) Visual cortex imaging field-of-view. Two example sessions. **Left:** VIP-tdTomato mouse injected with GCaMP8f. All neurons express GCaMP8f; a subset is in red, labeling VIP interneurons. Red and yellow: VIP interneurons. Green: non-VIP neurons, i.e., presumptive excitatory neurons. **Right:** SST-cre mouse injected with cre-dependent GCaMP8f. Green: SST interneurons.

D) Same as C, but for PPC.

E) Example fluorescence traces for excitatory, VIP, and SST neurons.

F–H) Mice received three paradigms (session types) distinguished by their ISIs. **Left:** distribution of ISIs in a session. **Right:** ISIs for example consecutive trials in a session. **F)** Short/long sessions had alternating blocks of trials with short (1s; blue) and long (2s; green) ISIs. **G)** Fixed/jittered sessions had alternating blocks of trials with fixed (1.5s; red) and jittered (0.5–2.5s; blue) ISIs. Each block also included 4% deviant ISIs (0.5s and 2.5s, black). **H)** In random sessions all trial ISIs were randomly chosen from a uniform distribution (0.5–2.5s).

I) Clustering methodology. **1)** <u>GLM model:</u> neural responses across the full session were modeled with a GLM using stimuli as input. **2)** <u>TRF model:</u> two temporal-receptive-field model variants, with opposite input polarity, were applied to the pre- and post-stimulus components of each kernel to get the ramp-up and ramp-down model responses, respectively. Goodness-of-fit comparisons determined whether each neuron was classified as ramp-up or ramp-down. **3)** <u>K-means clustering:</u> finally, neurons within each class were clustered using K-means on the TRF model parameters.

In temporal processing, too, inhibitory neurons play a role: SST interneurons are required for sequential population activity in both motor (Adler et al., 2019) and prefrontal cortex (Abbas et al., 2018). Particularly relevant to the present study is the ramping activity—observed in most VIP and some excitatory neurons—prior to an *expected* stimulus. Importantly, this ramp continues even further, when that stimulus is omitted (Garrett, Groblewski, Piet, Ollerenshaw, Najafi, et al., 2023; Garrett et al., 2020; Najafi et al., 2025).

Disambiguating temporal signaling from predictive processing. Temporal processing and temporal predictive processing can co-occur; however, their computational requirements differ. Predictive processing relies on learned internal models and therefore suggests that prediction signals should strengthen with experience. Temporal signaling, in contrast, can arise intrinsically from recurrent or synaptic dynamics and should be present even in naïve animals exposed to irregular stimulus statistics.

Many experimental paradigms entangle these processes. Regularly repeated stimuli simultaneously provide temporal signals and high predictability, making it difficult to attribute neural responses—such as ramping before a predictable event or activity after an unexpected sensory omission—to one mechanism or the other. Disambiguating these mechanisms is crucial for identifying the true computational role of neural circuits and for distinguishing intrinsic dynamics from learned predictive processing.

Present Study. We devised a three-stage paradigm in awake, head-fixed mice to tease apart temporal predictive processing and temporal signaling while performing two-photon calcium imaging of layer 2/3 excitatory, VIP, and SST neurons in medial visual cortex (VIS) and PPC. Across all experiments, mice passively viewed repeating audio-visual stimuli (0.2 s), separated by inter-stimulus intervals (ISIs)—neutral gray screen and no sound—whose durations varied according to the paradigm design.

1. Random ISI sessions: naïve mice received stimuli at uniformly distributed ISIs (0.5–2.5 s). High temporal variability minimizes timing predictions. Interval-dependent activity is therefore primarily attributed to temporal processing.

2. Fixed/Jittered ISI sessions: blocks of trials with fixed ISI (1.5 s)—hence fully predictable—alternated with blocks of jittered ISIs (0.5-2.5 s). Both blocks included occasional deviant ISIs (0.5 or 2.5 s: shorter or longer than expected), representing temporal prediction errors. Predictive processing predicts weaker anticipatory and prediction-error signals under jitter, whereas temporal processing should encode interval length regardless of variability.

3. Short/Long ISI blocks: mice experienced trial blocks alternating between 1-s or 2-s fixed ISIs, allowing us to test whether block transitions elicited prediction-error responses, and whether new temporal predictions emerged within each block.

Results. Across all three paradigms, neural dynamics in VIS and PPC were best accounted for by temporal signaling rather than predictive processing. Neurons clustered into two major categories—stimulus-activated (ramp-down) and stimulus-inhibited (ramp-up)—with subtypes defined by distinct rise and decay kinetics. Their activity shifted immediately at transitions between short and long blocks, inconsistent with gradual prediction updating. Deviant intervals in fixed versus jittered blocks elicited no differential responses, and the same functional clusters were present even in naïve animals exposed to random intervals. Decoding analyses revealed that heterogeneous kinetics across neurons generate a distributed population code for interval timing. Together, these findings establish that passive stimulus-evoked dynamics in VIS and PPC reflect intrinsic elapsed-time signaling, not temporal predictive processing.

Significance. These results resolve longstanding ambiguities by showing that ramping dynamics—previously interpreted as predictive signals in visual cortex—instead reflect stimulus-evoked activity whose intrinsic evolution encodes elapsed time. More broadly, they underscore the importance of incorporating carefully designed jittered paradigms before attributing ramping or omission-related activity to prediction or prediction-error signals. Key next steps are to: **(1)** dissect the cellular and synaptic mechanisms underlying intrinsic temporal codes in cortex; **(2)**

identify the circuits that implement temporal predictive processing during passive perception; and **(3)** determine whether, in perceptual decision tasks, VIS/PPC dynamics remain signatures of elapsed time or shift toward predictive coding.

Results

Paradigms to disentangle temporal signaling from temporal predictive processing

Neural signals during the interval between two events could reflect either of two processes (**Fig. 1A**): **(1)** the elapsed time since the previous event (temporal signaling), or **(2)** the expected timing of the next event (temporal predictive processing). These processes unfold concurrently, making it difficult to determine which function a neural circuit represents. Disentangling them is essential, because they rely on distinct underlying computations, and failing to do so risks misinterpreting circuit function.

To address this, we designed three paradigms to separate temporal signaling from predictive processing. Awake, head-fixed mice passively viewed a stream of repeating audio-visual stimuli (0.2 s), separated by an inter-stimulus interval (ISI; 0.5–2.5 s) (**Fig. 1B**; ISI includes gray screen and no auditory stimulus). Each stimulus consisted of a simultaneous auditory tone (11 kHz) and visual grating (whole-field static black/white stripes). Two-photon calcium imaging, via GCaMP8f (Zhang et al., 2023), was performed from the medial visual cortex (VIS; area PM, also termed V2M) and the posterior parietal cortex (PPC; area VISa) (**Supp Fig. 1**). Layer 2/3 excitatory neurons and VIP interneurons were simultaneously imaged in one cohort, and SST interneurons were imaged in a separate cohort of mice (VIP-Cre;Ai14 mice and SST-Cre mice injected with GCaMP8f; **Fig. 1C–E**).

The three paradigms were short/long, fixed/jittered, and random sessions (**Fig. 1F–H**).

- In short/long sessions, two block types alternated (50 trials each): ISI was fixed at 1 s in short blocks and 2 s in long blocks (**Fig. 1F**).
- In fixed/jittered sessions, two block types alternated (200 trials each): ISI was fixed at 1.5 s in fixed blocks, and randomly drawn from a uniform 0.5–2.5 s distribution in jittered blocks (**Fig. 1G**). Each block also contained 4% deviant ISIs (short deviant: 0.5 s; long deviant: 2.5 s). Deviants carried high surprisal in fixed blocks, while in jittered blocks they lay within the expected ISI range.
- In random sessions, all ISIs were independently drawn from a uniform distribution (0.5–2.5 s; **Fig. 1H**).

Importantly, naïve mice were first exposed to the random sessions, before experiencing the short/long and fixed/jittered paradigms. This design allowed us to examine neural responses to random intervals in animals without prior exposure to our stimuli.

Figure 2. VIS and PPC neurons demonstrate stimulus-evoked and ramping dynamics to repeating audio-visual stimuli. Data from the long block of short/long sessions. Clusters were identified on pooled neurons across all short/long sessions. **VIS:** top panels; **PPC:** bottom panels.

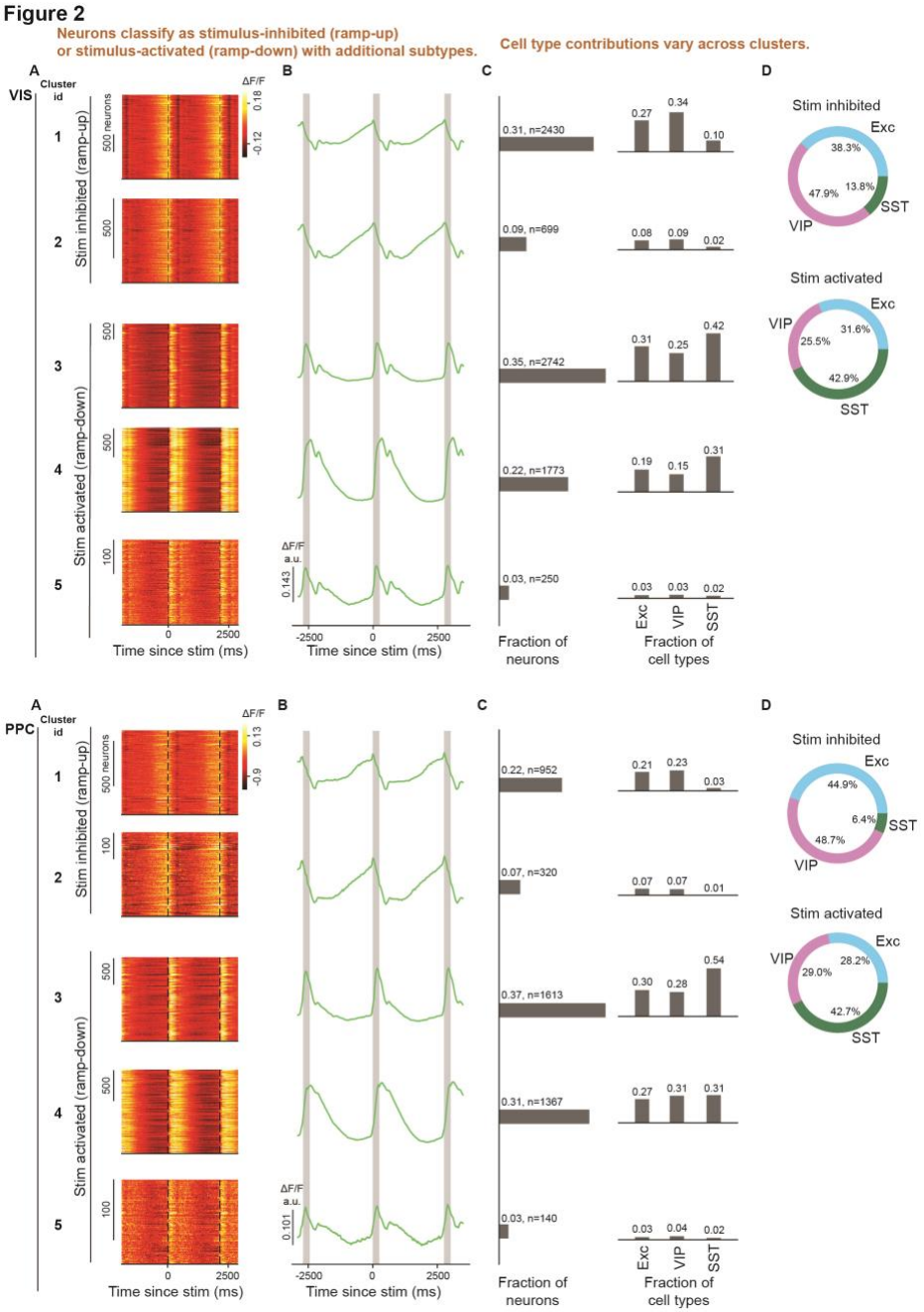

A) Heatmaps show trial-averaged, single-neuron activity (ΔF/F) for each cluster (top to bottom). The stimulus-inhibited (ramp-up) and stimulus-activated (ramp-down) labels on the left are based on the temporal-receptive-field (TRF) model outcome; the subtypes within each group (heatmap) are identified by k-means clustering applied on TRF model parameters (Fig. 1I).

B) ΔF/F, mean ± SEM across neurons and trials, for each cluster (top to bottom). Gray boxes: stimuli.

C) Left: fraction of all neurons assigned to each cluster. **Right:** fraction of neurons of each cell type assigned to each cluster.

D) Fraction of cell types within each broad class of stimulus-inhibited (top), and stimulus-activated (bottom).

VIS and PPC neurons demonstrate stimulus-activated and ramping dynamics to repeating audio-visual stimuli

We measured the response of excitatory, VIP, and SST neurons in VIS and PPC during passive audio-visual stimulation, using two-photon calcium imaging. The same field-of-view was imaged across days to enable direct comparison of neural responses across the three paradigms.

Neurons in both areas showed diverse response profiles (**Fig. 2A**), hence we clustered them into functional subtypes (**Fig. 1I**).

To perform clustering, we first modeled single-neuron responses using a generalized linear model (GLM). We then fit an ex-Gaussian temporal receptive field (TRF) model (Affan et al., 2025; Cao et al., 2024) to the GLM-derived stimulus kernel to extract response parameters such as ramp speed, and temporal width (**Fig. 6C,E; Supp Fig. 3; Supp Fig. 6**). These parameters were then clustered using k-means to define functional subtypes. Approximately 10% of neurons did not meet the TRF model inclusion criteria and were therefore excluded from the main figures. However, their response profiles were consistent with all results reported in this study (**Supp Fig. 4**).

Two broad clusters emerged: stimulus-inhibited (**Fig. 2A-C**; rows 1-2) and stimulus-activated (**Fig. 2A-C**; rows 3-5) neurons. Stimulus-inhibited responses typically evolved into a gradual ramp-up, whereas stimulus-activated responses evolved into a gradual ramp-down. Accordingly, we also refer to these clusters as ramp-up and ramp-down neurons, respectively. Both clusters contained subtypes with distinct response dynamics: stimulus-activated neurons ranged from fast/narrow to slow/broad responses (**Fig. 2B**; rows 3-5), while stimulus-inhibited neurons differed in ramp onset and amplitude (**Fig. 2B**; rows 1-2).

Stimulus-activated clusters with slow/broad peaks were more frequent in the PPC (**Fig. 2C** left; rows 4-5; 25% VIS neurons vs. 34% PPC neurons), whereas VIS contained more stimulus-inhibited ramp-up clusters (**Fig. 2C** left; rows 1-2; 40% VIS neurons vs. 29% PPC neurons).

The prevalence of slow stimulus-driven clusters in PPC aligns with the role of higher-order associative areas in perception (Avanzini et al., 2016). The presence of ramp-up clusters in PPC confirms and extends previous reports of ramping neurons in V1 and higher visual area LM (Garrett et al., 2020; Najafi et al., 2025).

Excitatory and inhibitory subtypes contributed to all clusters, but to varying degrees. SST neurons were most prevalent in stimulus-activated clusters (Garrett, Groblewski, Piet, Ollerenshaw, Najafi, et al., 2023) (**Fig. 2C** right**, 2D**). In contrast, a substantial fraction of VIP and excitatory neurons was stimulus-inhibited (Garrett, Groblewski, Piet, Ollerenshaw, Najafi, et al., 2023) (**Fig. 2C** right**, 2D**).

Interval transitions evoke immediate and stable neural response changes, inconsistent with temporal predictive processing

To study how VIS/PPC responses encode distinct intervals, we compared neural activity between short- and long-ISI blocks in the short/long paradigm (**Fig. 1F**; short ISI: 1 s; long ISI: 2 s). All clusters showed distinct activity patterns between the two blocks (**Fig. 3A-C**; blue: short block; green: long block). Stimulus-activated clusters exhibited smaller response amplitudes during the short-ISI block (**Fig. 3B**; rows 3-5). Stimulus-inhibited clusters differed in ramp amplitude and kinematics across short/long blocks (**Fig. 3B**; rows 1-2): clear ramps were observed in the long block, whereas the same neurons appeared much less responsive during the short block (**Fig. 3B**; rows 1-2).

Figure 3

Larger stimulus-evoked and ramping responses occur in long-interval blocks.

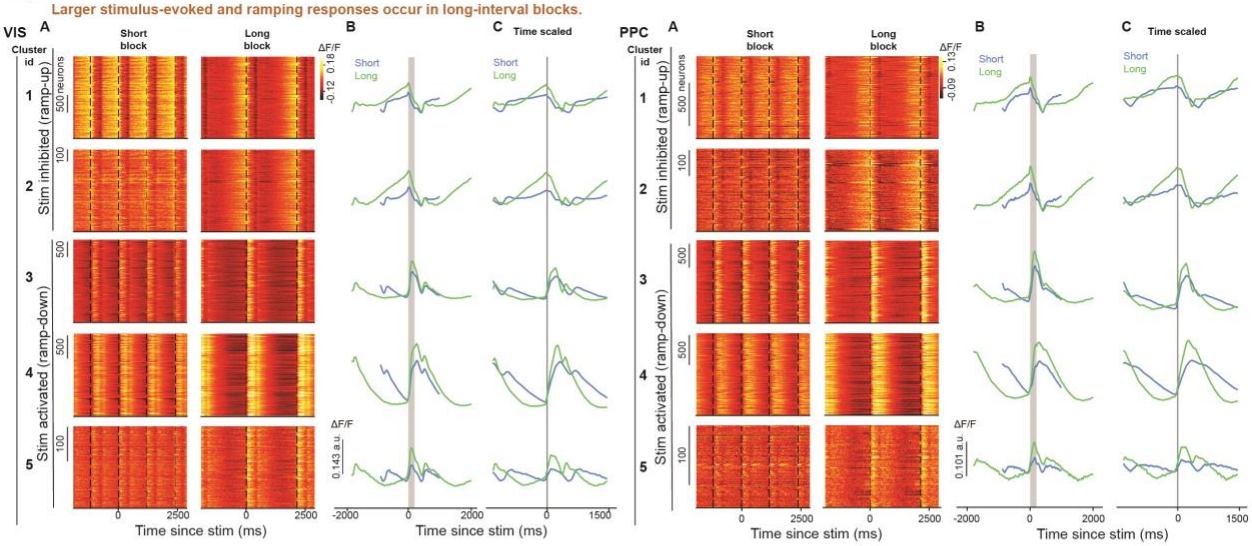

Neural responses change immediately with short/long block switches.

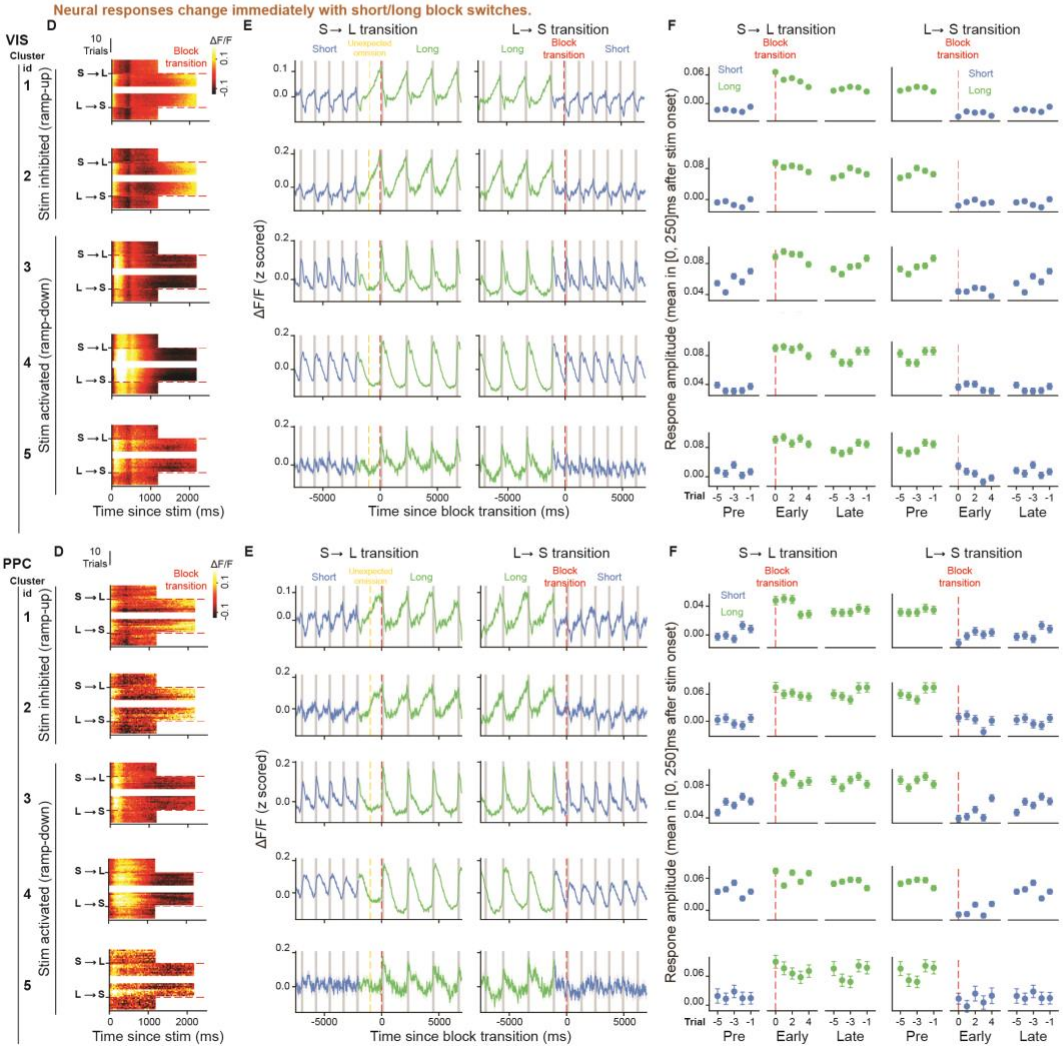

298

Figure 3. Interval transitions evoke immediate neural response changes that remain stable throughout the block. Data from the short/long sessions, comparing responses after short vs. long intervals (**A-C**; VIS: left panels; PPC: right panels), and demonstrating rapid response changes after block transitions that remain stable within the block (**D-F**; VIS: top panels; PPC: bottom panels. Clusters are the same as in Fig. 2. Each row corresponds to a cluster.

A) Heatmaps of trial-averaged, single-neuron activity aligned on stimuli (vertical lines) in the short (**Left**) and long (**Right**) ISI blocks, for each cluster (top to bottom). Neurons are sorted identically for short and long blocks.

B) Neuron- and trial-averaged activity for short (blue) and long (green) blocks, aligned on the stimulus (gray box).

C) Same as B, but with the time axis scaled to place short and long on the same timescale.

D) Heatmaps of trial-by-trial, population-averaged activity around block transitions (red horizontal lines), for both short-to-long (S→L) and long-to-short (L→S) block switches, for distinct clusters (top to bottom). Rows: individual trials.

E) Trial-by-trial neural activity around block transitions. Same as **C**, but shown as line plots (mean ± SEM across neurons and blocks). Red line: first stimulus after ISI switch for both transitions. Yellow line: expected stimulus timing based on the short block (first unexpected stimulus omission). Blue: short block; Green: long block. Gray boxes: stimuli.

F) Response magnitude quantified in the 300ms window after stimulus onset, for 5 trials before transition (pre), 5 trials immediately after (early), and the last 5 trials of the block (late).

We next examined how responses changed following block transitions (**Fig. 3D-F**). All clusters showed immediate adjustments on the first trial after the transition, with minimal further change thereafter. Following short-to-long transitions, stimulus-activated clusters increased response amplitude on the very first long-ISI trial (**Fig. 3E,F left**; rows 3-4), while stimulus-inhibited clusters exhibited much more pronounced ramps, already evident in the first long-ISI (**Fig. 3E,F left**; rows 1-2). The opposite effects were observed during long-to-short transitions, with stimulus-activated clusters decreasing in amplitude and stimulus-inhibited clusters showing attenuated ramps (**Fig. 3E,F right**).

To quantify these dynamics, we measured response magnitude across three epochs: immediately before a block transition, immediately after, and late within the block (Pre, Early, Late, respectively; **Fig. 3F**). This analysis confirmed that neural responses across all clusters changed immediately after interval transitions and remained generally stable within each block (**Fig. 3F**). While a subset of stimulus-activated clusters showed slight amplitude drifts during the final trials of a block (**Fig. 3F**, VIS: row 3; PPC: rows 3,4), these gradual changes appear to reflect slow baseline shifts in fluorescence and were far smaller than the abrupt response changes observed at block transitions.

The predictive-processing hypothesis posits that a change in interval at block transitions should generate a temporal prediction error, which would gradually diminish within a block as new temporal predictions emerge. Our results contract this:

After short-to-long transitions, stimulus-inhibited clusters exhibited activity changes at the time of the unexpectedly omitted stimulus in the first long ISI (**Fig. 3E left**; yellow line), which could superficially resemble a prediction-error signal. However, the magnitude and timing of ramps remained stable across subsequent long-interval trials (**Fig. 3E,F left**). Conversely, during long-to-short transitions, stimulus-inhibited neurons did not respond to the first short-ISI trial, and stimulus-activated neurons showed reduced response amplitude (**Fig. 3E right**; redline). Also, no further changes were observed during subsequent trials after the transition (**Fig. 3E right**).

The absence of any transient prediction-error response or gradual adaptation (**Fig. 3E**; yellow and red lines), together with the immediate and stable nature of these changes, argues against temporal predictive-processing mechanisms.

Fixed vs. jittered ISI blocks confirm absence of temporal predictions and temporal prediction errors in VIS/PPC

While our short/long-session results do not support temporal predictive processing, alternative explanations could be considered. One possibility is that neurons encode only long-ISI prediction errors, since some activity changes coincided with stimulus omissions (**Fig. 3E**; rows 1,2: yellow line). Another is that the absence of change after short-to-long transitions reflects co-occurring signals within the same neurons—prediction signals that gradually increase and prediction-error signals that gradually decrease—effectively canceling each other. Finally, for long-to-short transitions, an unusually high learning rate could allow predictions to be updated in a single trial, explaining the absence of gradual adaptation.

To test these scenarios more directly, we ran fixed/jittered-ISI block sessions (**Fig. 1G**). Fixed blocks consisted of constant ISIs (1.5 s) with occasional unexpected short or long intervals (deviants: 0.5 s and 2.5 s). In jittered blocks, ISIs were drawn from a uniform 0.5–2.5 s distribution, so the same 0.5 s and 2.5 s intervals were expected. Predictive processing therefore predicts stronger temporal prediction-error responses to deviant ISIs in fixed compared to jittered blocks, as well as stronger temporal prediction signals in fixed blocks due to temporal regularity.

Surprisingly, and in clear contrast to predictive-processing predictions, responses to deviant ISIs were indistinguishable between fixed and jittered blocks, for both short and long deviants (**Fig. 4A,E**: long, short deviants, respectively; Red: fixed; Blue: jittered). This key result provides strong evidence against temporal prediction-error coding in PPC or VIS during passive audio-visual stimulation. Ramp-up neurons likewise showed no difference across fixed and jittered contexts (**Fig. 4A,E**; rows 1-2; see ramps prior to stimulus at t=0), inconsistent with ramping activity representing temporal prediction signals, which should have weakened under jitter.

A potential counter-argument is that both block types shared the same mean ISI (1.5 s), so average ramp dynamics might overlap despite differences in trial-to-trial variability. To address this, we computed a single-trial modulation index to quantify responses to unexpected events—specifically, stimulus omissions during long deviants and unexpected stimulus deliveries during short deviants (including the stimulus immediately following a long deviant)—and compared its distribution between the two block types (**Supp Fig. 2**). However, we found no differences

between fixed and jittered blocks, whether in response mean or variance, for either long or short deviants (**Supp Fig. 2**; Mean comparison: two-tailed Mann–Whitney U test; Variance comparison: two-tailed Levene's test; Significance threshold: $p < 0.05$).

Figure 4

Responses to unexpected stimulus omission or delivery are identical across fixed and jittered temporal contexts.

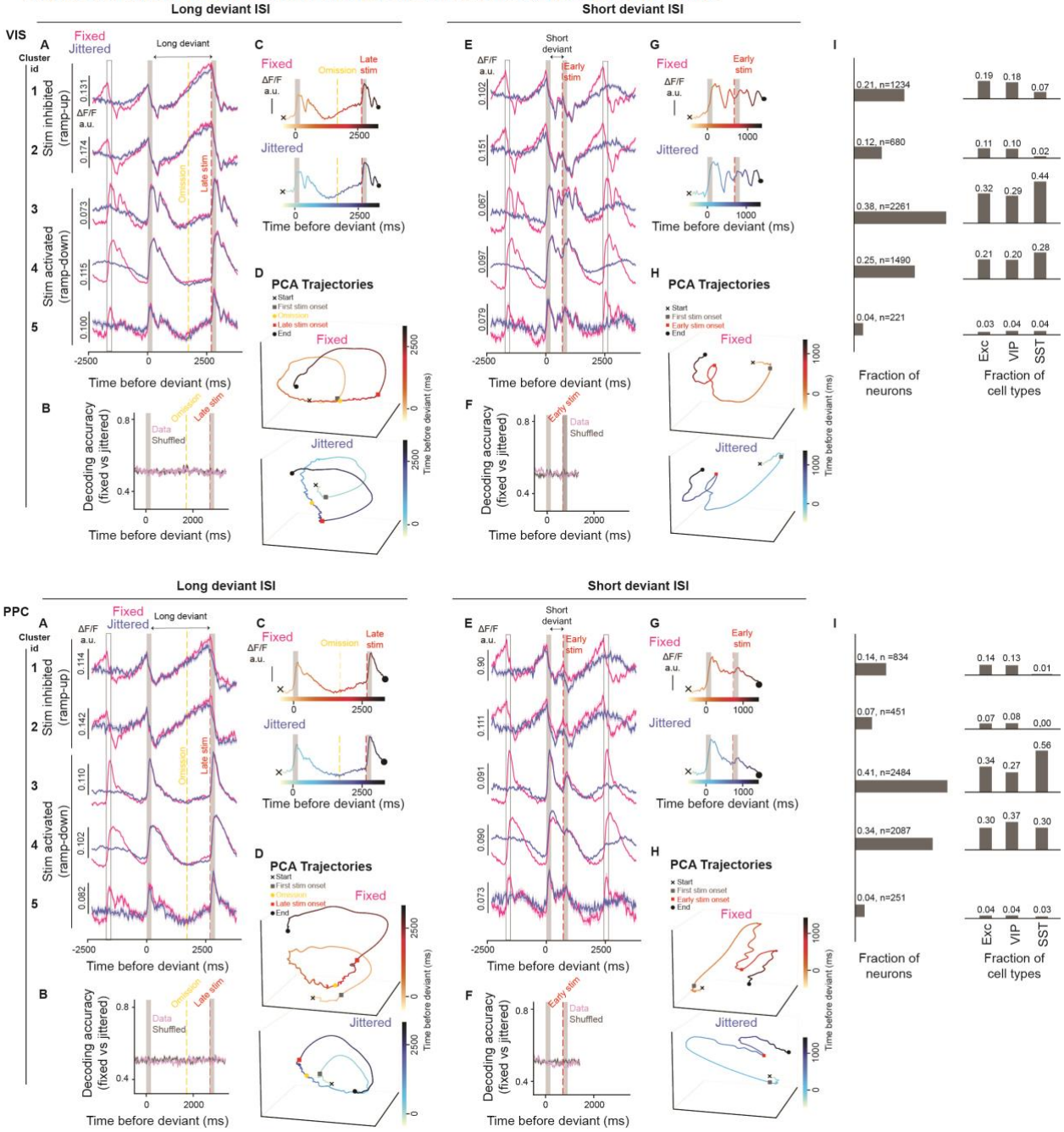

Figure 4. Neural responses do *not* differ between fixed and jittered ISI blocks for either long or short deviant ISIs. Data from fixed/jittered sessions, showing identical responses to both short and long deviant ISIs across fixed and jittered blocks. Clusters were identified on pooled neurons across all fixed/jittered sessions. **VIS:** top panels; **PPC:** bottom panels.

A) Neural responses (mean ± SEM) for each cluster, for fixed (red) and jittered (blue) blocks, aligned on the stimulus before the long deviant ISI (yellow line: expected but omitted stimulus; Gray boxes: stimuli; Empty boxes: stimuli in fixed and mean stimuli time in jittered).

B) Decoding accuracy for classifying fixed vs. jittered trials (cross-validated; Purple: real data; Gray: shuffled data; Yellow line: omission).

C) Population average, across all neurons of all clusters, for fixed (top) and jittered (bottom) blocks, aligned on the long deviant ISI. Traces are color-coded to match PCA trajectories in D.

D) PCA population trajectories for fixed (top) and jittered (bottom) trials, aligned on the long deviant ISI (projection on top 3 PCs); Yellow: unexpected omission, due to the long ISI; Red: unexpected late stimulus (stimulus after the long deviant ISI).

E–H) Same as A–D, but aligned on the stimulus after short deviant ISI. Red: unexpected early stimulus (stimulus after the short deviant ISI).

I) Left: fraction of all neurons assigned to each cluster. **Right:** fraction of neurons of each cell type assigned to each cluster, for fixed/jittered sessions.

To test whether subtle differences might be obscured in mean responses, we trained a linear decoder to classify fixed versus jittered trials based on activity around deviant ISIs (**Fig. 4B**). Decoder performance remained at chance, providing further evidence that responses to deviants were indistinguishable between fixed and jittered conditions (**Fig. 4B,F**: long and short deviants, respectively; Purple: data; Gray: shuffled control).

Finally, we performed principal component analysis (PCA) to examine how population trajectories change during unexpected events in both fixed and jittered contexts (**Fig. 4C,G**: population averages; **Fig. 4D,H**: projection on top 3 principal components; Yellow line/box: unexpected stimulus omission during long deviants; Red line/box: unexpected stimulus delivery after a deviant ISI). In both contexts, stimulus onset drove trajectories to an evoked state, which then gradually relaxed back (**Fig. 4D**, gray square: pre-deviant-ISI stimulus).

Importantly, in the fixed block, unexpected omissions (**Fig. 4D** top; yellow: omission) did not perturb the trajectory, which continued in state space until the next stimulus (**Fig. 4D** top; red: late stimulus), closely resembling the jittered trajectory (**Fig. 4D**, bottom). Also, the late stimulus following the deviant ISI, despite its unexpected timing, produced a trajectory similar to that evoked by the predictable stimulus before the deviant ISI (**Fig. 4D**, gray vs. red squares), and this similarity was observed in both fixed and jittered conditions (**Fig. 4D**: PCA; **Fig. 4C**: population averages).

A similar lack of difference was observed for short deviants: in both fixed and jittered contexts, the post-deviant stimulus ("early stimulus," **Fig. 4G,H**; red) pushed trajectories into an evoked state. Compared to the stimulus before the short deviant (**Fig. 4H**; gray), this early stimulus produced a smaller trajectory change, consistent with the reduced response amplitudes in short versus jittered blocks (**Fig. 3B**).

Ramping activity arises from intrinsic sensory dynamics not learned predictions

To determine whether ramping responses depend on prior experience with regular stimulus timing, we examined naïve mice that had never been exposed to our task paradigms. These animals viewed the same audio-visual stimuli presented at random ISIs, eliminating any temporal regularity or learned expectation.

We observed the same neuronal clusters—stimulus-activated and inhibited—even in naïve mice (**Fig. 5**). Strikingly, ramp-up neurons were already present from the very first session (**Fig. 5C**). To address the possibility that rapid predictions might emerge within the first day, we compared neural responses between the first 100 and last 100 stimuli of day 1, but again found no difference (**Fig. 5D**; black: first epoch; blue: last epoch). Finally, the prevalence of clusters remained generally stable across days (**Fig. 5E**).

Across all paradigms, our evidence argues that neural responses—and particularly the ramp-ups—are not related to temporal prediction signals. A key question, then, is what underlies the response changes observed during short/long interval block switches (**Fig. 3E**), or following short/long deviant ISIs (**Fig. 4**). To address this, we binned the random intervals and examined how responses varied across distinct interval lengths (**Fig. 5F**).

Stimulus-activated responses were similar across interval bins, but their relaxation (ramp-down) was truncated when the next stimulus occurred early (**Fig. 5F;** rows 4-5; green shades) and extended further when the next stimulus was delayed (**Fig. 5F**; rows 4-5; orange/pink). Likewise, the ramp-up in stimulus-inhibited clusters was interrupted if a stimulus occurred early, whereas it continued further when the next stimulus was delayed (**Fig. 5F**; rows 1-3; Green shades: shorter bins; Orange/pink: longer bins). <u>Thus, neural responses across ISI bins appeared as different snapshots of the same underlying dynamic, interrupted and reset whenever the next stimulus arrived</u> (**Fig. 5F**).

Population trajectory analysis confirmed this view (**Fig. 5H**, projection on top 3 principal components): trajectories followed a common path across all intervals, simply evolving further along the same trajectory until reset by the next stimulus (**Fig. 5H**; random ISIs divided into 10 bins; Trajectories start at stimulus onset and end at the mean ISI bin).

To examine how long ramping activity can persist, we extended the random-ISI paradigm to longer intervals (3-7.5 s; **Supp Fig. 5**). Ramp-up activity increased monotonically for the first ~4 s after stimulus onset before reaching an apparent plateau (**Supp Fig. 5C,D**), likely reflecting both circuit-level and measurement effects.

Together, these results indicate that VIS and PPC dynamics reflect intrinsic relaxation processes reset by each stimulus, rather than adaptation or prediction-error mechanisms.

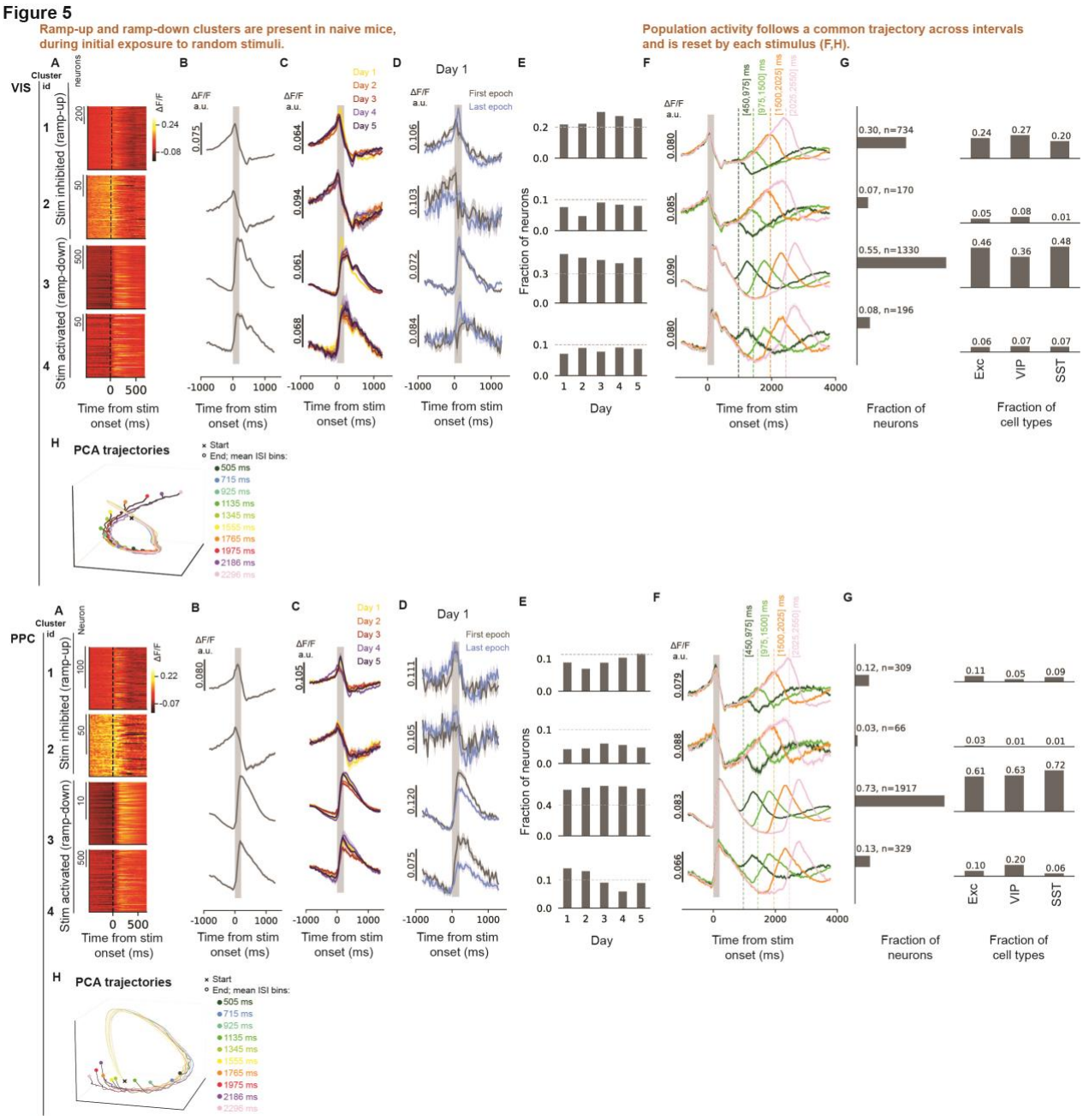

Figure 5. Neural ramps during repeating stimuli are intrinsic and reflect self-evolving sensory dynamics. Data from random sessions, showing that all neural clusters are present from the beginning in naïve mice, and do not require learning to emerge. Clustering was performed on pooled neurons across all random sessions. Each row corresponds to a cluster. **Top panels:** VIS; **Bottom panels:** PPC.

A) Heatmaps of trial-averaged, single-neuron activity aligned on stimulus onset (black line), for each cluster (top to bottom).

B) Neuron- and trial-averaged responses aligned on the stimulus (gray box) for each cluster.

C) Averaged responses aligned on the stimulus, same as **B**, but shown separately for individual random

sessions (different colors).

D) Averaged responses for the first (gray) and last (blue) 100 trials of the first session.

E) Fraction of total neurons in each cluster distributed across the five random days.

F) Random ISIs divided into four bins (different colors). Neural responses averaged across trials within each ISI bin. Gray box: stimulus. Vertical lines: mean ISI of each bin.

G) Left: fraction of all neurons assigned to each cluster. **Right:** fraction of neurons of each cell type assigned to each cluster.

H) PCA of population activity (projection on top 3 components) from stimulus onset through the ISI. Random ISIs were divided into 10 bins (210 ms each), and trajectories are shown up to the mean ISI for each bin. Trajectories follow a common path across intervals and extend further along it with longer ISIs.

Heterogeneous rise/decay kinetics enable population coding of time

Our results so far demonstrate that post-stimulus activity reflects the unfolding of intrinsic cortical dynamics (**Fig. 5F,H**), independent of predictive processing (**Fig. 3E,4**). We next asked what information these ramps might carry—specifically, whether they encode elapsed time (**Fig. 1A**). We reasoned that the diversity of rise and decay kinetics across neurons (**Fig. 2A,B**) should support a population code for time: neurons with different temporal profiles would peak at distinct moments, collectively spanning a wide range of intervals.

To assess this, we trained a decoder to discriminate pairs of time bins based on population activity within each cluster (**Fig. 6B**; binary linear SVM trained on long-block data from the short/long sessions: **Fig. 6A**). Neurons within each cluster were subsampled to the same count to allow unbiased cross-cluster comparison. All clusters carried information about elapsed time, but their decoding profiles differed systematically (**Fig. 6B,D**; chance at 50%). Stimulus-activated clusters decoded short intervals more accurately, with high initial accuracy that declined over time (**Fig. 6B**: rows 3-5; **Fig. 6D**: green, cyan, blue). In contrast, stimulus-inhibited clusters showed stable decoding throughout the interval, with a small increase in accuracy near the end, consistent with their ramp-up dynamics (**Fig. 6B**; rows 1-2; **Fig. 6D**: orange, red).

To understand how response kinematics shape these profiles, we compared parameters of the temporal-receptive-field model across clusters (**Fig. 6C,E**). A clear pattern emerged: clusters with faster and narrower responses supported higher temporal precision (**Fig. 6D,E**; green; cyan), whereas clusters with slower and broader responses provided more stable decoding (**Fig. 6D,E**; blue; orange; red).

Altogether, our findings support a simple mechanistic model: stimulus onset resets the population into an evoked state that then relaxes toward baseline. Both the rise into the evoked state and the decay back vary across neurons. This diversity in response kinetics enables the population to represent elapsed time across multiple scales. Accordingly, changes in neural responses across ISIs reflect sampling different phases of a shared trajectory, rather than adaptive or predictive mechanisms.

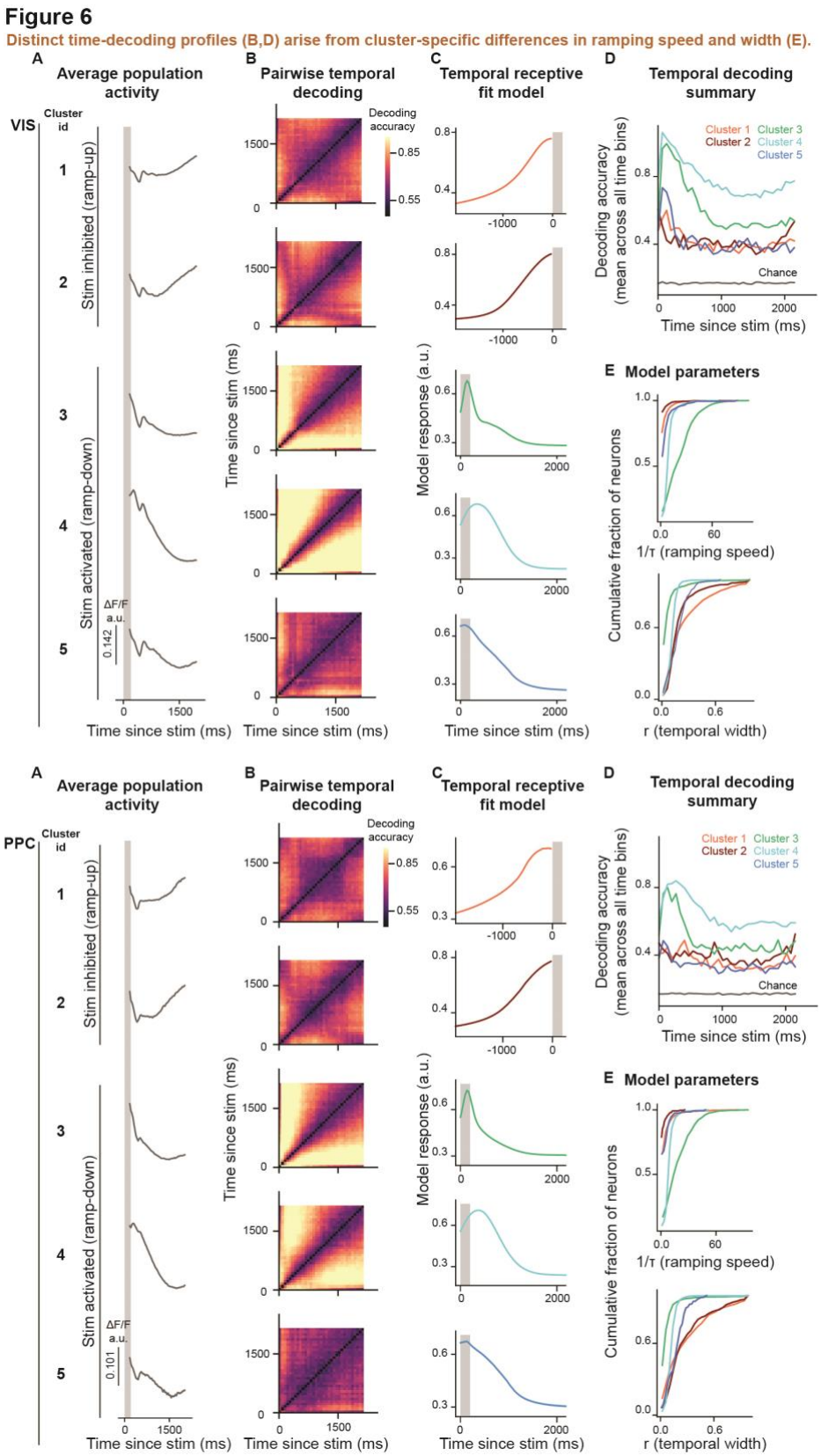

Figure 6. Heterogeneous ramp kinetics enable population coding of time. Data from the long block of short/long sessions, showing heterogeneous kinetics across clusters, which leads to distinct temporal coding profiles across the interval. Clusters are the same as in Fig. 2. Each row corresponds to a cluster. **Top panels:** VIS; **Bottom panels:** PPC.

A) Mean population activity, shown for each cluster (top to bottom).

B) Pairwise classification accuracy matrices (cross-validated). Each cell shows the accuracy for distinguishing a given pair of time bins, shown for each cluster. Cluster sizes were matched by neuron subsampling to enable cross-cluster comparison.

C) Temporal receptive field model response (see Fig. 1I), averaged across neurons, shown for each cluster. Orange, red: ramp-up clusters. Green, cyan, blue: ramp-down clusters.

D) Mean pairwise decoding accuracy at each time point, obtained by averaging panel B across all time bins, excluding the diagonal. Orange, red: ramp-up clusters. Green, blue, cyan: ramp-down clusters.

E) Distribution of model parameters across neurons within each cluster; Top: ramping speed (1/τ); Bottom: temporal width (r). Distinct decoding profiles (B, D) arise from cluster-specific differences in ramping speed and temporal width.

Discussion

During passive presentation of repeated audio-visual stimuli in awake mice, neurons in the medial visual cortex (VIS) and posterior parietal cortex (PPC) segregated into two main functional categories: stimulus-activated (ramp-down) and stimulus-inhibited (ramp-up) cells. Within each category, subtypes were distinguished by their ramp kinetics, spanning fast to slow temporal profiles **(Fig. 2)**. Three findings showed that these ramps were independent of temporal prediction or prediction-error processes: **(1)** neural activity changed immediately across blocks with short and long inter-stimulus intervals (ISIs; **Fig. 3**); **(2)** responses immediately before expected stimuli and after unexpected onset shifts were identical in fixed and jittered blocks (**Fig. 4**); and **(3)** the same functional clusters were present in naïve mice during fully random ISIs (**Fig. 5**).

Analysis of responses as a function of interval length (**Fig. 5F**) showed that apparent differences across short and long intervals simply reflect the intrinsic evolution of stimulus-evoked activity, rather than responses to omitted or predicted events. Decoding analyses further revealed that these clusters collectively encode elapsed-time information, with each cluster's interval preference determined by its characteristic ramp kinetics (**Fig. 6**).

Together, these findings demonstrate an intrinsic, distributed representation of elapsed time across VIS and PPC during passive viewing—emerging from the self-evolving dynamics of sensory responses rather than from temporal prediction or learning mechanisms. Whether mice actually read out this temporal information remains unknown—our paradigm was passive and provided no behavioral report. Nevertheless, the fact that time can be linearly decoded from these trajectories suggests that downstream circuits could access this intrinsic signal to estimate time, even in the absence of explicit task demands to attend to time.

Visual omission responses: comparison with prior studies

Our findings demonstrate that ramping activity after unexpected visual-stimulus omissions reflect neither temporal expectation nor temporal prediction-error signals (Garrett, Groblewski, Piet, Ollerenshaw, Najafi, et al., 2023; Garrett et al., 2020; Najafi et al., 2025; Nitzan & Buzsáki, 2025), but rather the intrinsic evolution of stimulus-evoked activity and its relaxation back toward baseline. Moreover, although behavioral variables may co-vary with omissions (Najafi et al., 2025), our results show that they are not the cause of these responses—fundamentally, there is no discrete "omission response", only the continuation of ongoing dynamics.

A key distinction between this and prior studies lies in **how *temporal predictive processing* and *omissions* are defined**. Here, temporal prediction refers specifically to the brain's estimate of *when* the next stimulus will occur. We manipulated this by jittering the duration of a neutral gray interval between otherwise identical stimuli—holding stimulus identity and duration constant—to isolate timing-related processes without confounding changes in visual content or duration.

In contrast, image-sequence-based studies (Knudstrup et al., 2025; Price et al., 2023) have defined an "omission" as repeating the previous image instead of presenting the next.

Consequently, prediction errors in these paradigms reflect violations of both stimulus identity and duration within a learned image sequence. Robust omission effects in those studies emerge only after multi-day training—specifically, exposure to the sequence without deviants following an initial reference session (Knudstrup et al., 2025)—indicating sequence-specific learning.

Our paradigm, by contrast, employs simple repeated-image presentations and defines omission as a prolonged neutral-gray period, thus probing *timing per se* without changes in stimulus identity or duration. Importantly, even after repeated daily exposure to sessions containing rare omissions, we did not observe the emergence of omission-related activity, suggesting that these dynamics do not depend on learning the session's temporal structure. While we cannot entirely rule out that omission responses might emerge if animals were first trained on sessions without omissions, we consider this unlikely given the very low omission rate in our paradigm and the absence of a complex image sequence that could support such learning.

Other studies have examined omissions in closed-loop visuomotor contexts, where visual flow is coupled to locomotion (Fiser et al., 2016; Furutachi et al., 2024; Zhang et al., 2025). In those tasks, omission events—replacing an expected image with gray—represent violations of *sensorimotor contingencies* rather than purely temporal predictions. Thus, while the term "omission" is shared, the underlying predictive computations differ fundamentally.

A recent study most comparable to ours (Nitzan & Buzsáki, 2025), reanalyzed large-scale Allen Institute datasets and concluded that omission responses in visual cortex do not represent prediction errors, but may instead reflect temporal expectation or rebound activity. Our results extend these insights using a dedicated experimental design that directly dissociates elapsed-time encoding from prediction. By systematically varying interval regularity and experience, we confirm that visual cortical activity neither signals temporal prediction errors nor predictions themselves. Rather, ramping dynamics reflect intrinsic, time-evolving processes within local circuits.

Taken together, these observations emphasize the need for precise definitions of "omission" and "temporal predictive processing" when designing experiments and interpreting omission-related activity across sensory and behavioral contexts.

Possible sites of temporal predictive processing during visual perception

A pressing question raised by our findings is where in the brain temporal predictive processing during passive visual inputs is implemented (Coull et al., 2011). Hippocampal neurons—and subcortical regions such as the thalamic medial geniculate nucleus—have been suggested to carry temporal prediction-error signals, since, compared to the gradual ramps observed in visual cortex, they exhibit steeper responses to visual omissions (Nitzan & Buzsáki, 2025).

Another potential candidate is the cerebellum. Numerous studies have established its role in encoding timing and error signals during sensorimotor behavior (Boven et al., 2025; Gao et al., 2018 Li 2018; Garcia-Garcia et al., 2024; Giovannucci et al., 2017; Herzfeld & Lisberger, 2025; Medina & Mauk, 2000; Najafi & Medina, 2013; O'Reilly et al., 2008; Ohmae et al., 2017; Shadmehr et al., 2010; Suvrathan et al., 2016). Fewer studies have examined the cerebellum's

role during passive stimulation (Najafi et al., 2014), but evidence shows that the cerebellum is active following unexpected omissions of passive somatosensory stimuli (Tesche & Karhu, 2000) and is necessary for detecting temporal mismatches during passive auditory inputs (Moberget et al., 2008). With respect to visual inputs, the cerebellum encodes repeated visual stimuli and their omissions during motor behavior (Kameda et al., 2019), but its role during passive visual perception remains to be determined.

Other candidate regions for temporal predictive processing include the basal ganglia (Kameda et al., 2019; Matell et al., 2003; Mello et al., 2015) and the prefrontal cortex (Kim et al., 2013; Wang et al., 2018; Xu et al., 2014), alongside the auditory cortex, whose role in auditory temporal predictive processing is well established (Jaramillo & Zador, 2011; Schneider et al., 2018; Yaron et al., 2024).

VIS/PPC, too, may reflect temporal prediction signals but in active perceptual paradigms where animals need to attend to stimuli to receive reward. Human EEG studies support this view: anticipatory signals were absent during passive rhythmic streams but emerged when subjects prepared for action (Breska & Deouell). Future studies using paradigms similar to ours, but including active perceptual or behavioral contexts, will be critical for determining whether VIS and PPC dynamics shift from elapsed-time coding toward predictive processing. Also, several animal studies have reported predictive and error signals in cortical areas when sensory events are behaviorally relevant (Chubykin et al., 2013; Cole et al., 2024; Hockley et al., 2025; Jordan & Keller, 2020; Najafi et al., 2020; Shuler & Bear, 2006). This implies that task engagement may be necessary to recruit temporal predictive processing in these circuits.

The importance of incorporating jittered stimuli when interpreting predictive processing results

A common approach for studying temporal predictive processing is to present stimuli at regular intervals. However, in such paradigms, temporal prediction signals often overlap with elapsed-time signals, which reflect the time since the previous stimulus. This overlap makes it difficult to determine whether neural activity reflects prediction or simple temporal tracking.

Our fixed/jittered paradigm with deviant ISIs, together with the random-ISI paradigm in naïve mice, provide a powerful tool to separate elapsed-time signaling from temporal predictive processing. <u>Without these paradigms, neural responses to long-ISI deviants (omissions) could be mistakenly interpreted as temporal prediction errors, and ramping signals as temporal predictions.</u>

The predictive processing framework suggests that: **(1)** Deviant ISIs should generate stronger prediction errors in fixed blocks compared to jittered blocks, and temporal predictions should be stronger in fixed blocks. **(2)** Naïve mice exposed for the first time to random intervals should not exhibit temporal predictions. **(3)** In short/long-ISI sessions, temporal prediction errors should arise at block transitions, leading to gradual within-block adaptation and updating of predictions.

Our data contradict all of these predictions: **(1)** We observed no differences between fixed and jittered blocks, for either standard or deviant ISIs (**Fig. 4**). **(2)** Neural subtypes, including

ramping clusters, were indistinguishable between naïve and experienced mice (**Fig. 5**). **(3)** No gradual adaptation followed block transitions; instead, responses changed immediately (**Fig. 3**).

Our results demonstrate that ramping and omission responses—in visual and parietal cortices during passive stimulation—are not temporal prediction signals but the intrinsic evolution of stimulus-evoked activity (**Fig. 5**) that carries linearly decodable information about elapsed time (**Fig. 6**). Similar "population clock" dynamics have been described across brain regions (Mauk & Buonomano, 2004; Xu et al., 2014; Yu et al., 2022), indicating that temporal coding can arise intrinsically from network dynamics without prediction or reinforcement.

Interval representation emerges from stimulus-reset attractor dynamics

Our results can be understood within an attractor-dynamics framework (Hennequin et al., 2018; Rajan et al., 2010; X.-J. Wang, 2008), in which each stimulus pushes neurons from baseline into a transient evoked state, after which activity relaxes back toward baseline. In this view, responses differ across interval lengths not because of trial-by-trial learning, but because the same intrinsic trajectory is **reset** and restarted at different points in its cycle.

This framework naturally accounts for our key findings: **(1)** the immediate changes in neural responses at block transitions (**Fig. 3**) without invoking trial-by-trial learning; **(2)** identical responses between fixed and jittered ISI contexts (**Fig. 4**), despite lower predictability in the jittered case and weaker deviant responses; and **(3)** the presence of the same neural clusters in both naïve and experienced mice (**Fig. 5**).

Importantly, this view situates our results within a broader attractor literature. Stimulus-reset attractor dynamics have been linked to variability quenching at onset (Churchland et al., 2010; Hennequin et al., 2018) and to persistent activity in working-memory and decision circuits (Inagaki et al., 2019; Wang et al., 2023; X. J. Wang, 2008). Our findings extend this framework to interval signaling: stimulus onsets place VIS/PPC populations onto reproducible evoked trajectories whose cluster-specific kinetics tile elapsed time, thereby yielding a learning-independent population code for interval duration (Murray et al., 2014; Paton & Buonomano, 2018).

Diverse neuronal dynamics provide a distributed code for time

Neurons in VIS and PPC showed heterogeneous dynamics after stimulus presentation: both the rise into the evoked state and the decay back to baseline varied across cells. Some stabilized at baseline after recovery (**Fig. 2**; rows 3,4), consistent with fixed-point attractors, whereas others gradually drifted over time (**Fig. 2**; row 5), consistent with manifold-like dynamics in which the attractor landscape is shallow enough to allow slow evolution in state space rather than collapse to a single fixed point. This heterogeneity aligns with reservoir models of diverse timescales, where variable neuronal kinetics create overlapping trajectories that together form a distributed population code for elapsed time (Bernacchia et al., 2011; Buonomano & Maass, 2009; Murray et al., 2014; Paton & Buonomano, 2018; Wang et al., 2018).

Evidence for such diverse (Affan et al., 2025) timescales extends across brain systems: in the cerebellum, granule cells provide heterogeneous temporal kernels important for interval learning (Barri et al., 2022; Garcia-Garcia et al., 2024; Medina & Mauk, 2000); in the striatum, medium spiny neurons exhibit sequential dynamics that tile time over seconds (Matell et al., 2003; Mello et al., 2015); and in the hippocampus, “time cells” fire at distinct delays from an event, collectively spanning behavioral intervals (MacDonald et al., 2011; Pastalkova et al., 2008).

The diversity of rise and decay dynamics effectively provides a set of temporal filters in which each neuron is tuned to a different portion of the interval. In this sense, the population acts like a basis set: overlapping response profiles that can be flexibly combined downstream to reconstruct elapsed time. Such an organization enhances robustness to noise, since time is represented redundantly, and allows different circuits to emphasize narrow or broad signals depending on task demands. This framework parallels basis-function models of time in recurrent networks and supports the view that elapsed time is encoded through a distributed population code rather than by a single dedicated mechanism (Buonomano & Maass, 2009; Laje & Buonomano, 2013; Paton & Buonomano, 2018).

Contrast with temporal scaling models

Our findings complement but also diverge from the temporal scaling framework described in behaving animals and recurrent network models (De Corte et al., 2022; Wang et al., 2018). Temporal scaling emphasizes that the same population trajectory can be flexibly stretched or compressed in time, with trajectory speed adjusted to represent short versus long intervals.

By contrast, our data show that passive interval coding in VIS and PPC does not arise from scaling a common trajectory: responses to short and long intervals were not scaled versions of one another. Instead, each neuron contributes a fixed trajectory defined by its own timescale, and stimuli presented at different intervals reset these trajectories at different phases. Thus, while both frameworks support the idea that time is encoded in evolving population activity rather than by a dedicated clock, our results point to a distributed tiling of intrinsic trajectories rather than flexible rescaling of a single one.

Cell-type-specific mechanisms underlying heterogeneous neural dynamics

While all cell types contributed to each functional cluster, there were notable cell-type-specific biases. SST neurons were predominantly stimulus-activated, whereas excitatory and particularly VIP neurons were more prevalent in the stimulus-inhibited cluster (**Fig. 2D**). Given that our stimuli were presented at high contrast, these results are consistent with prior findings (Millman et al., 2020) showing that SST neurons preferentially respond to high contrast, whereas VIP interneurons and layer 2/3 excitatory neurons are more responsive to low contrast. The stimulus-inhibited (ramp-up) neurons observed here could reflect bottom-up inputs from circuits containing *suppressed-by-contrast* cells (Masland & Martin, 2007) previously described in the retina (Rodieck, 1967) and thalamus LGN (Piscopo et al., 2013), or alternatively, modulation by top-down influences such as behavioral state, reinforcement, or neuromodulatory drive (Fu et al., 2015; Pi et al., 2013; Shin & Adesnik, 2021; Szadai et al., 2022; Tremblay et al., 2016).

The heterogeneous rise and decay dynamics we observe can be explained by a combination of intrinsic, synaptic, circuit, and modulatory mechanisms, with E/I (excitatory/inhibitory) motifs playing a key role in shaping this diversity, as outlined below.

At the intrinsic level, neurons differ in their ion channel composition, such that strong A-type K^+ currents drive rapid repolarization and narrow responses, while persistent Na^+ or slow Ca^{2+} currents sustain activity and generate broader responses (Hodgkin & Huxley, 1952; Marder & Goaillard, 2006).

Synaptic inputs also vary in their filtering properties: differences in release probability, vesicle pool size, and receptor kinetics produce characteristic time constants, with some synapses showing rapid depression and others facilitation, and receptor subtypes (e.g., AMPA vs. NMDA, GABA A vs. GABA B) contributing fast or slow components (Abbott & Regehr, 2004; Zucker & Regehr, 2002).

Beyond single-cell properties, the E/I balance in recurrent circuits amplifies this diversity, as neurons within inhibitory-dominated loops recover quickly, while those in excitatory-rich loops maintain activity longer.

Finally, neuromodulators further shape kinetics in a cell-type-specific manner: acetylcholine recruits VIP interneurons to gate inhibition in VIS (Fu et al., 2015; Pi et al., 2013), noradrenaline broadens integration times and enhances ramping dynamics (Sara & Bouret, 2012), and dopamine adjusts recurrent integration in prefrontal networks (Seamans & Yang, 2004).

The larger response amplitudes observed during long-ISI blocks, across excitatory, SST, and VIP populations (**Fig. 3B**), likely arise from recovery processes operating on sub-second to multi-second timescales. Longer intervals allow partial restoration of synaptic and circuit resources depleted by repeated stimulation. Mechanistically, this could reflect replenishment of vesicle pools following synaptic depression (Tsodyks & Markram, 1997), relaxation of activity-dependent gain control that suppresses network responses at short ISIs (Carandini & Heeger, 2012), recovery from intrinsic spike-frequency adaptation that limits excitability at short intervals (Benda & Herz, 2003), and recovery of PV/SST synaptic transmission, leading to stronger transient inhibition and consequently larger rebound responses in excitatory neurons at longer intervals (Beierlein et al., 2003). Together, these slow restorative dynamics can account for the interval-dependent amplitude scaling without invoking predictive or learning-based mechanisms.

Limitations of the study

We restricted our analyses to layer 2/3 neurons in VIS and PPC. Other cortical layers, particularly layer 5, may contribute more directly to predictive computations since they integrate top-down and thalamic inputs (Harris & Shepherd, 2015; Maristany de las Casas et al., 2025; Vélez-Fort et al., 2014). Our cell-type coverage was also limited to excitatory, SST, and VIP neurons. Other inhibitory populations such as NDNF interneurons—shown to disinhibit PV cells and gate long-range inputs in layer 1—likely shape predictive signals and could play a role in temporal predictive processing (Abs et al., 2018; Ibrahim et al., 2021).

In addition, we used two-photon calcium imaging, which provides only an indirect proxy of spiking activity. The slow kinetics of calcium indicators blur fast transients, potentially biasing the estimation of timescales and attenuating high-frequency components of neural responses (Wei et al., 2020; Zhang et al., 2023).

While stimulus orientation was varied across tens of trials, the present study focused specifically on temporal structure rather than stimulus identity. Our findings therefore do not address prediction or prediction-error signals related to *what* stimulus appears, but only those related to *when* it appears.

VIS localization. Viral injections were targeted to medial visual cortex using stereotaxic coordinates. Post-hoc histology confirmed GCaMP expression in the medial part of the visual cortex (area PM) (**Supp Fig. 1**, top). PM is considered a higher visual area with a preference for higher spatial frequencies and lower temporal frequencies (Marshel et al., 2011; Zhuang et al.).

Although response properties can differ across visual areas, our initial experiments (unpublished data) targeting the primary visual cortex (V1) yielded similar results to those observed in the medial visual cortex in this study. Taken together with the lack of difference between the medial visual cortex and PPC—an associative area linking stimulus and action—we therefore consider it unlikely that our core finding (stimulus-reset ramps invariant to temporal predictability) depends on the precise visual subarea. Yet, additional experiments directly targeting V1 could further clarify its role in temporal predictive processing.

Discussion summary

Neural dynamics in VIS/PPC during passive audio-visual stimulation do not support temporal predictive processing. Instead, they are consistent with intrinsic stimulus-reset relaxation dynamics whose diverse timescales enable distributed temporal signaling. Other brain regions, such as the hippocampus and the cerebellum, remain potential candidates for temporal predictive processing during passive behavior. Finally, prior work suggests that active engagement, involving top-down inputs and reward contingencies, can recruit prediction and error signals in sensory areas, raising the testable hypothesis that task demands may shift visual/parietal responses from intrinsic elapsed-time coding toward explicit temporal predictive processing.

Methods

Subjects

Female and male transgenic mice were used in the current study. Mice included VIP-tdTomato and SST-cre (Jackson 013044) lines. VIP-tdTomato line was produced by breeding VIP-cre (Jackson 031628) with Ai14 (Jackson 007914; cre-dependent tdTomato). All procedures were approved by the Institutional Animal Care and Use Committee at the Georgia Institute of Technology and agreed with guidelines established by the National Institutes of Health.

855
856 **Sample size and statistical tests**

857 Ten mice (female and male) were used: 5 for PPC imaging and 5 for VIS imaging. 18,904 VIS
858 neurons and 14,835 PPC neurons were imaged across all sessions (**Table 1**). ~10% neurons
859 did not pass temporal-receptive-field modeling criteria (see below) and were excluded from the
860 main figures but quantified in **Supp Fig. 4**.

861 Two-tailed Mann–Whitney U test, and two-tailed Levene's test were used to compare
862 distribution means and variances, respectively. Statistical significance was defined as $p < 0.05$.

Region	Cell type	Random	Fixed/jittered	Short/long	Total
VIS	Excitatory	2,226	5,634	7,101	**14,961**
	VIP	597	692	1,233	**2522**
	SST	181	600	640	**1421**
	Total	**3,004**	**6,926**	**8,974**	**18,904**
PPC	Excitatory	2,437	5,327	3,913	**11,677**
	VIP	304	678	401	**1,383**
	SST	319	839	617	**1,775**
	Total	**3,060**	**6,844**	**4,931**	**14,835**

863
864 **Table 1.** Number of imaged neurons per brain region, cell type, and paradigm.
865

866 **Behavioral paradigms**

867 Head-fixed mice were seated in a half-cylindrical tube (The International Brain et al., 2021), and
868 received 3 session types (behavioral paradigms): random, fixed/jittered, and short/long
869 sessions. Each mouse received 5 random sessions, followed by 10–15 fixed/jittered sessions,
870 and then 10–20 short/long sessions. All sessions contained ~2,000 audiovisual stimuli.

871 • In random sessions, ISIs were drawn from a uniform distribution (0.5–2.5 s).
872 • In fixed/jittered sessions, 5 fixed blocks and 5 jittered blocks were presented: blocks of 200
873 trials alternated between fixed ISIs (1.5 s) and jittered ISIs (uniform distribution: 0.5–2.5 s).
874 Total of 4% of ISIs in fixed/jittered sessions were 'deviant', evenly split between short- and
875 long-deviant ISIs.
876 • In short/long sessions, 19 short blocks and 19 long blocks were presented: blocks of 50
877 trials alternated between short ISIs (1 s) and long ISIs (2 s).

878
879 **Stimulus design**

880 Auditory and visual stimuli were always presented simultaneously and lasted 200 ms on each
881 repetition. The ISI was defined as the absence of the auditory stimulus accompanied by a
882 neutral gray screen.

883 Auditory stimulus was an 11 kHz pure tone. Visual stimuli were full-field, static sinusoidal
884 gratings of four orientations (0°, 45°, 90°, 135°), at spatial frequency 0.08 cycles/degree. Visual

885 stimuli were displayed on a monitor (Dell, G2524H; 1920x1080 pixels), set to 100% contrast and
886 75% brightness and covered with a blue screen filter (Amazon) to minimize imaging artifacts
887 during stimulus presentation. The monitor was positioned to the right side of the mouse, with
888 placement parameters following previous literature (de Vries et al., 2020; Juavinett et al., 2017).

889 The same grating orientation was presented for 15-20 consecutive trials before switching to
890 another randomly-selected orientation. Orientation changes did not occur for 3 trials
891 immediately after transitioning to a new block (in both fixed/jittered and short/long sessions) or
892 for 3 trials at the end of each block. Stimulus orientation changes were not analyzed in this
893 study.

894

895 **Surgical procedure: window craniotomy**

896 Stereotaxic surgeries (David Kopf, Instruments; Models 942 and 1900) were performed under
897 isoflurane inhalation anesthesia (Somno; Kent Scientific). Anti-inflammatory drug
898 Dexamethasone (1-2mg/kg) was subcutaneously injected 24h and 1h before the surgeries.
899 Post-op care involved subcutaneous injection of the analgesic drug Ketoprofen (2-5 mg/kg).
900 During the surgery, 0.1-0.2mL sterile saline was Intraperitoneally (IP) injected to compensate for
901 liquid loss.

902 A circular craniotomy in 3mm diameter using a biopsy punch (Fischer Scientific) was made over
903 the left PPC (Najafi et al.) (stereotaxic coordinates: 2mm posterior to bregma, 1.7mm lateral) or
904 the left VIS (Georgia Bastos et al.) (stereotaxic coordinates: 2.92mm posterior to bregma,
905 2.0mm lateral).

906 Injection pipettes (15-20 um in diameter; Drummond Micropipettes 3.5") were back-filled with
907 mineral oil (Sigma Aldrich) and then front-filled with viral vectors: AAV9-Syn-jGCaMP8f
908 (Addgene #162376) for VIP-tdTomato mice, and AAV1-CAG-flex-jGCaMP8f (Addgene #162382)
909 for SST-cre mice. Virus titers was 2.3 x 10^13 gc/mL, and they were both 2-10X diluted in sterile
910 saline. Virus injections were made (Nanoject III; Thomas Scientific) with the speed 10nl/sec in 3-
911 4 different locations (within 1mm around the coordinate center), each with 500nl virus, and ~150
912 um below the dura.

913 A glass plug—made by stacking a 3mm coverslip and a 5 mm coverslip with optical bond
914 (Norland Optical Adhesive NOA 81; Edmund Optics)—was used to cover the craniotomy
915 window. Vetbond (Amazon) and metabond (C&B Metabond® Quick Adhesive Cement System;
916 Parkell Inc.) were used to seal the craniotomy window. Black cement (Ortho-Jet BCA) was
917 applied to reduce possible light leakage during optical imaging.

918

919 **Two-photon calcium imaging**

920 Two-photon calcium imaging data were acquired using a Bruker Ultima 2Pplus laser-scanning
921 microscope (Tunable laser set at 920nm: Spectra-Physics Mai Tai High Power DeepSee—Nikon
922 objective: 16X; NA 0.8—Chroma emission filters: 520/40-2p for the green channel and 660/40-
923 2p for the red channel). All imaging experiments were conducted in darkness. The microscope

objective was immersed in water-based ultrasonic gel, and the objective was covered with black electrical tape to minimize light leakage.

After surgical recovery, mice were habituated to the setup for 1–2 days before imaging sessions commenced. The same field of view was imaged across days to enable direct comparison of neural responses across the three paradigms. Each imaging session lasted ~1 hour. During each session, calcium imaging videos (512 × 512 pixels, 30 Hz), stimulus voltage traces (10 kHz), and high-speed videos of the mouse's left eye were recorded (30 Hz; FLIR camera; Lens: CM3-U3-13Y3M-CS 16mm; each video frame triggered by the imaging scope).

Preprocessing imaging data

We used a customized pipeline based on suite2p (Pachitariu et al., 2017) to extract neurons and their activity from the imaging videos. Raw videos were imported into suite2p to identify regions of interest (ROIs) and their raw fluorescence traces. All parameters were kept at the software's default settings.

As an initial quality control step, ROIs with a compactness value greater than 1.06 were excluded to remove poorly segmented ROIs with abnormal geometry. For each trace, a Gaussian filter ($\sigma = 600s$) was applied to estimate the fluorescence baseline and compute ΔF/F as $\frac{(F_{fluo}-F_{base})}{F_{base}}$, where F_{fluo} is the raw fluorescence signal and F_{base} is the extracted baseline from the Gaussian filter. Finally, each neuron's ΔF/F trace was z-scored individually.

Identification of VIP interneurons

We used the 'cellpose' algorithm (Stringer & Pachitariu, 2025) to identify VIP interneurons labeled with tdTomato in the red channel. For each segmented ROI, we collected the corresponding functional mask from the green channel and quantified red–green co-localization with an overlap score based on intersection-over-union as $s = \frac{|R \cap G|}{|R \cup G|}$, where R and G are the tdTomato and GCaMP masks, respectively. Neurons were then classified as excitatory ($s \leq 0.3$), uncertain ($0.3 < s < 0.7$), or VIP ($s \geq 0.7$). Here, the two thresholds (0.3, 0.7) were chosen a priori based on empirical validation.

Temporal receptive field (TRF) model

We modeled single-neuron temporal responses around a stimulus using an ex-Gaussian temporal receptive field (TRF) model (**Fig. 1I; Fig. 6C,E; Supp Fig. 3; Supp Fig. 6**). The model has been successfully used to analyze the neural ramping dynamics in the anterior lateral motor cortex (Affan et al., 2024), medial prefrontal cortex (Cao et al., 2024), and entorhinal cortex (Bright et al., 2020). A similar model also has been used to reveal sequential firing in hippocampus and prefrontal cortex (Cruzado et al. 2020).

This model, denoted as $TRF(t) = (G * E)(t)$, is defined as

$$TRF(t; b, a, m, r, \tau) = b + \frac{a}{2}\exp\left(\frac{2m+r^2}{2\tau} - \frac{t}{\tau}\right) erfc\left(\frac{m+\frac{r^2}{\tau}-t}{\sqrt{2}r}\right),$$

where $erfc$ denotes the error function. This form results from convolving a Gaussian kernel G:

$$G(t; m, r) = \frac{1}{\sqrt{2\pi}r}\exp\left(-\frac{(t-m)^2}{2r^2}\right),$$

with a causal exponential decay E:

$$E(t; \tau) = \frac{1}{\tau}\exp\left(-\frac{t}{\tau}\right).$$

Here, $b \in \mathbb{R}$ is the baseline offset, $a > 0$ represents the absolute response amplitude, and $m \in \mathbb{R}$ denotes the response latency (mean of the Gaussian kernel). The parameter $r \in (0,1)$ controls temporal receptive field width, with smaller values yielding narrower Gaussian kernels. The exponential component is governed by $\tau > 0$, which sets the timescale of ramp-up or ramp-down. Responses with larger τ decay more slowly back to baseline. For interpretability, we use $\frac{1}{\tau}$ to represent ramping speed.

To fit the TRF model to a neuron (**Fig. 1I**), we aligned the neural activity during the interval before and the one after stimulus onset at $t = 0$. Time was normalized for fitting stability, denoted as $t_- \in [-1,0]^{n_1}$ and $t_+ \in [0,1]^{n_2}$, respectively, where n_1 and n_2 are the number of time points.

Let $x_- \in [0,1]^{n_1}$ and $x_+ \in [0,1]^{n_2}$ be the two segmentations of the normalized activity, referring to the pre-stimulus and post-stimulus activity, respectively. We then fit $TRF(-t; b, a, m, r, \tau)$ to x_- and fit $TRF(t; b, a, m, r, \tau)$ to x_+, which we refer to as ramp-up and ramp-down models, respectively (**Fig. 1I**). Note that both models have the same parameters, but they are fit to inputs of opposite direction (flipped in time). The ramp-up and ramp-down models differ only by the direction of the time input (forward vs reversed). This gives two sets of parameters $\theta_- = \{b_-, a_-, n_-, r_-, \tau_-\}$ and $\theta_+ = \{b_+, a_+, n_+, r_+, \tau_+\}$, referring to the *ramp-up* and the *ramp-down* model components. Note that this model always assumes that each neuron has both the ramp-up component, before stimulus, and ramp-down component, after stimulus. The goodness of fit is evaluated by the coefficient of determination between the prediction and the ground-truth normalized activity for both components.

Clustering neural responses

We used a combination of generalized linear modeling (GLM) (Garrett, Groblewski, Piet, Ollerenshaw, Najafi, et al., 2023; Steinmetz et al., 2019) and the TRF model prior to clustering (**Fig. 1I**). For each paradigm, neural responses from all sessions were pooled together, and the following steps were performed on the combined dataset.

1) GLM modeling. High-sampling-rate voltage recordings of the stimulus trace (10 kHz) were first aligned with the fluorescence traces, for the entire 1hr session, using nearest-neighbor interpolation. For each neuron, we fit a GLM to the z-scored ΔF/F trace $f \in \mathbb{R}^{N_{time}}$ using the

binary stimulus trace $S \in \{0,1\}^{N_{time}}$ as input, over the window $[-1500,1500]$ ms relative to stimulus onset (N_{time} denotes the number of imaging frames in a session, with 1 indicating stimulus presentation and 0 indicating no stimulus). This window was determined such that we can fit the TRF model easily for the incoming steps. To prevent overfitting and obtain smooth kernel estimates, we applied L2 regularization $\alpha = 5 \times 10^4$multiplier). The GLM kernel for the i-th neuron $k_i \in \mathbb{R}^{n_k}$ was then estimated via the least square principle $k_i = (S^T S)^{-1} S^T f$.

Next, since the fit convolution kernel is flipped from the actual GLM kernel, we flipped the resulting GLM kernel to correct this. We then split the fit GLM kernel k_i into two parts, $k_{i-}(t)$ with $t < 0$ and $k_{i+}(t)$ with $t > 0$, which are therefore the summaries of how a neuron generally responds before and after a stimulus, respectively.

2) TRF modeling. See the Methods section 'Temporal receptive field (TRF) model' for details. In brief, for each neuron, we fit 2 TRF models to the 2 components of the GLM kernel, $k_{i-}(t)\ and\ k_{i+}(t)$, corresponding to the ramp-up and ramp-down models, respectively:

$\theta_{(i)-} = \{b_{(i)-},\ a_{(i)-},\ n_{(i)-},\ r_{(i)-},\ \tau_{(i)-}\}_{i=1}^{N_{neuron}}$, and

$\theta_{(i)+} = \{b_{(i)+},\ a_{(i)+},\ n_{(i)+},\ r_{(i)+},\ \tau_{(i)+}\}_{i=1}^{N_{neuron}}$.

Let $R^2_{(i)-}$ and $R^2_{(i)+}$ denote the goodness of fit for the two models. We defined ramp-up neurons as the neurons that can fit (1) well with the ramp-up model, and (2) better than the ramp-down model, and vice versa. Let θ be the threshold ($\theta = 0.3$ in this paper).

Thus, those neurons with both $R^2_{(i)-} > \theta$ and $R^2_{(i)-} > R^2_{(i)+}$ are determined as the ramp-up neuron, while those neurons with both $R^2_{(i)+} > \theta$ and $R^2_{(i)+} > R^2_{(i)-}$are the ramp-down neuron. All other neurons with both goodness of fit lower than the threshold is not included in further analysis (~10%). Therefore, this thresholding serves the quality control procedure in this paper, resulting in N_{up} ramp-up neurons and N_{down} ramp-down neurons.

3) K-means clustering. After getting the two board categories of neurons, within each ramp-up and ramp-down group, we use k-means on the fit the temporal receptive field width parameters, $\{r_{(i)-}\}_{i=1}^{N_{up}}$ and $\{r_{(i)+}\}_{i=1}^{N_{down}}$, to find subgroup of neurons with distinct response dynamics. The number of clusters is determined such that the Silhouette Coefficient is maximized.

Time scaling analysis

To test for potential temporal scaling effects (**Fig. 3C**), we performed the following procedures. Let $t_{src} \in \mathbb{R}^{n_{src}}$ denote the original time stamps for an aligned neural trace and $t_{des} \in \mathbb{R}^{n_{des}}$ denote the target time range to which the trace was scaled, where n_{src} and n_{des} are the respective length of the time stamps. Scaled time stamps were computed as:

$t_{scaled} = \frac{t_{src}}{n_{src}} \times n_{des}$.

A nearest neighbor interpolation was then used to map t_{scaled} to t_{des}. This procedure left the neural activity values unchanged but adjusted the time axis to match the target interval. Given neural activity aligned to stimulus onset, we applied this scaling separately to the pre-stimulus and post-stimulus intervals, while leaving the activity during the stimulus itself unchanged.

Modulation index for deviant ISIs in fixed/jittered sessions

We quantified condition-evoked changes (**Supp Fig. 2**) with a symmetric modulation index defined as

$$m = \frac{v_{post} - v_{pre}}{|v_{post}| + |v_{pre}|} ,$$

where v_{pre} and v_{post} are the average signal within the pre- and post-event windows. This normalization bounds the index in $[-1,1]$, is invariant to overall scaling, and treats increases and decreases symmetrically ($m > 0$: relative increase after the event; $m < 0$: decrease; and $m = 0$ no change).

- Positive prediction error (stimulus after deviant ISI; **Fig. 4**, red dashed line; both short/long blocks): Responses were averaged over [0,300] ms relative to stimulus onset. v_{pre} was aligned to the pre-deviant stimulus, v_{post} to the post-deviant stimulus (**Supp Fig. 2**); hence, the modulation index reflects response modulation relative to the 'standard' stimulus.
- Negative prediction error (unexpected omission during long deviant ISIs; **Fig. 4**, yellow dashed line): $v_{pre}$was taken from the 300 ms preceding the expected stimulus, and v_{post} from the time of the expected stimulus onset; hence, the modulation index reflects response modulation relative to baseline immediately before the omission.

Population trajectory analysis

Neural population activity was analyzed in a low-dimensional latent space using principal component analysis (PCA). For each condition c_i (e.g., trials within the fixed block or jittered block in **Fig. 4D**, or trials within each ISI bin in **Fig. 5H**), we first averaged neural activity across trials to obtain a condition-specific response matrix: $X_{c_i} \in \mathbb{R}^{n_{neuron} \times n_{time}}$. These matrices were then concatenated across conditions to form a combined data matrix $X \in \mathbb{R}^{n_{neuron} \times (n_{time} \times n_{condition})}$. PCA was fitted to this combined dataset to extract the principal axes capturing the greatest shared variance across neurons and conditions. For visualization, population trajectories for each condition were obtained by projecting their time-varying population activity onto the top three principal components (PC1–PC3), which together defined a shared low-dimensional space for comparing neural dynamics across conditions. Each point along a trajectory thus represents the instantaneous population state at a given time, and its color encodes time progression.

To obtain smoother neural trajectories, each PC was interpolated to increase the number of time points fourfold, followed by Savitzky–Golay filtering (polynomial order = 3, window size = 8).

Temporal decoding analysis

To evaluate how neural populations encode elapsed time (**Fig. 6**), we trained classifiers to discriminate neural activity between pairs of time bins within an interval. Neural data were aligned to stimulus onset and truncated at the onset of the next stimulus. Each time bin was defined as two non-overlapping imaging frames, with neural activity averaged within each bin for every neuron and trial.

To reduce single-trial noise in calcium imaging, we used a bootstrapping approach: on each iteration (n=250), pseudo-trials were generated by averaging random subsets of three trials.

To control for population-size differences across clusters, neurons were randomly subsampled (n=25) to a fixed number (n = 120) in each bootstrap iteration. The resulting data tensor was denoted as:

$x \in \mathbb{R}^{n_{trials} \times n_{neurons} \times n_{time}}$, where n_{trials}, $n_{neurons}$, n_{times} are the number of pseudo trials, neurons, and time bins, respectively.

For each pair of time bins, pseudo-trials were split into training and test sets (80/20 split). A Support Vector Machine (SVM) classifier with a linear kernel was trained on data shaped as $n_{neurons} \times (n_{trials} \times n_{time})$. This train/test procedure was repeated 25 times using stratified randomized folds, which ensured that both time bins were equally represented in each split. The decoding accuracies from a total of $N_{trial\ bootstrp} \times N_{neuron\ subsample} \times N_{splits}$ repetitions (250 trial bootstraps, 25 neuron subsamples, and 25 splits) were averaged to provide a stable estimate. This procedure was repeated across all time-bin pairs, and the results were assembled into a time-by-time accuracy matrix: $ACC \in [0,1]^{n_{time} \times n_{time}}$.

Data and code availability

All data used in this paper will be made public upon the paper publication. Code for data processing and analysis is publicly available on Najafi Lab GitHub page: https://github.com/najafi-laboratory/2p_imaging/tree/main/passive_interval_oddball_202412

Acknowledgments

We are grateful to the Haider Lab for providing the SST-Cre mice, to Simone Russo for thoughtful discussions, to Laurence Copeland and Vanshika Mehta for assistance with early experiments, to Joey Broussard, Robert Howard, Leslie Claar, and Ben Ouellette for valuable technical expertise, and to Dieter Jaeger for helpful comments on our manuscript.

This work was supported by awards to F.N. from the Whitehall Foundation, the Research Corporation for Science Advancement (Scialog), and the Chan Zuckerberg Initiative (CZI).

Author contributions

Y.H.: Experiments; Data analysis; Conceptualization; Writing
A.S.: Clustering method (initial version); Help with figure preparation
M.C., S.W.: Help with imaging experiments
T.S.: Engineering support
S.M.: Histology
F.N.: Conceptualization; Writing; Supervision; Funding acquisition; Resources

Declaration of interests

The authors declare no competing interests.

Supplemental Figure 1

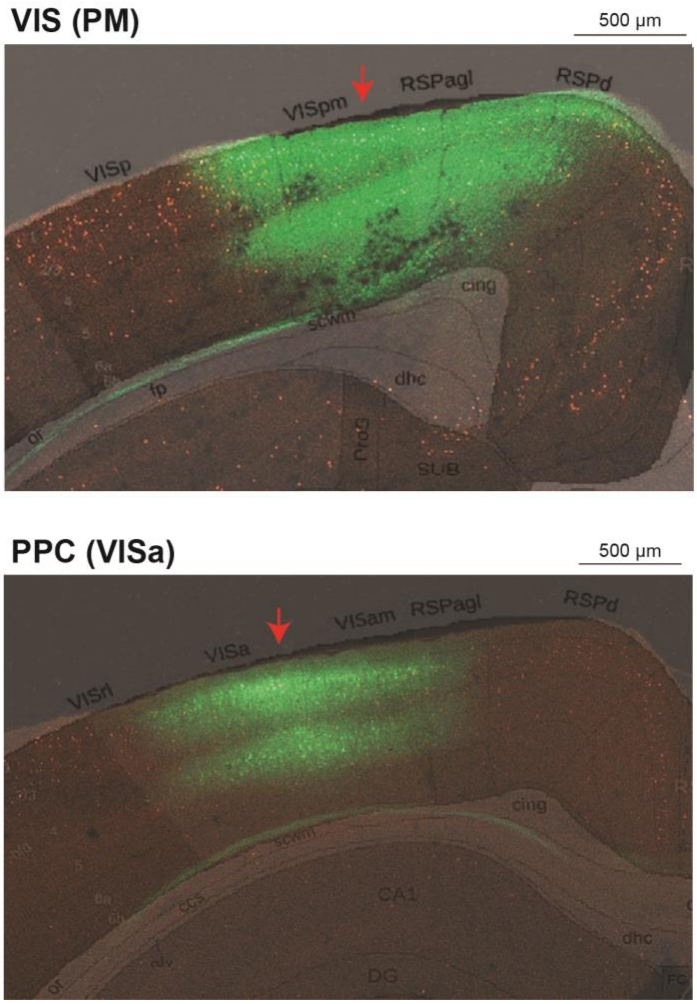

Supplemental Figure 1 (related to Fig. 1). Histological verification of imaging sites in the medial visual and posterior parietal cortex.

Histology images from two example mice (VIP-tdTomato) imaged in VIS (**top,** area PM) or PPC (**bottom**), with Allen coronal slices superimposed. Red arrow: center of craniotomy window used for imaging, marking VIS (PM), and PPC (VISa). Green: cells labeled by GCaMP8f injection. Multiple injections were performed within the 3-mm cranial window. Two-photon imaging was primarily conducted from the window center.

Supplemental Figure 2

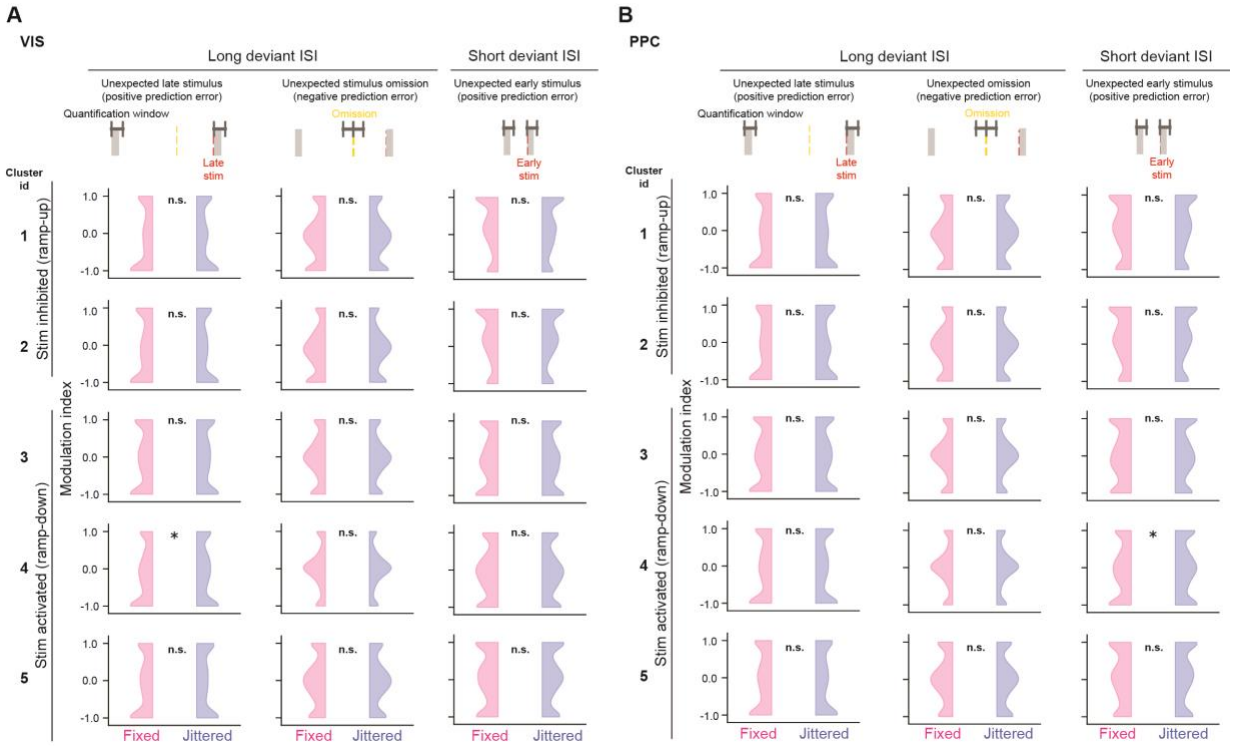

Supplemental Figure 2 (related to Fig. 4). Positive and negative prediction errors are represented similarly in fixed and jittered temporal contexts, ruling out temporal predictive processing as their underlying mechanism. **A)** VIS. **B)** PPC

Comparison of fixed (pink) and jittered (blue) block responses to unexpected events: late stimulus after a long deviant ISI (**left column**; Red line at the top schematic denotes the late stimulus, i.e., positive prediction error), stimulus omission during a long deviant ISI (**middle column**; Yellow line at the top schematic denotes the omission, i.e., negative prediction error), and early stimulus after a short deviant ISI (**right column**; Red line at the top schematic denotes the early stimulus, i.e., positive prediction error).

Response modulation was quantified with a modulation index (Methods) by comparing neural activity across the two quantification windows (horizontal bars at the top, 300 ms each).

Supplemental Figure 3

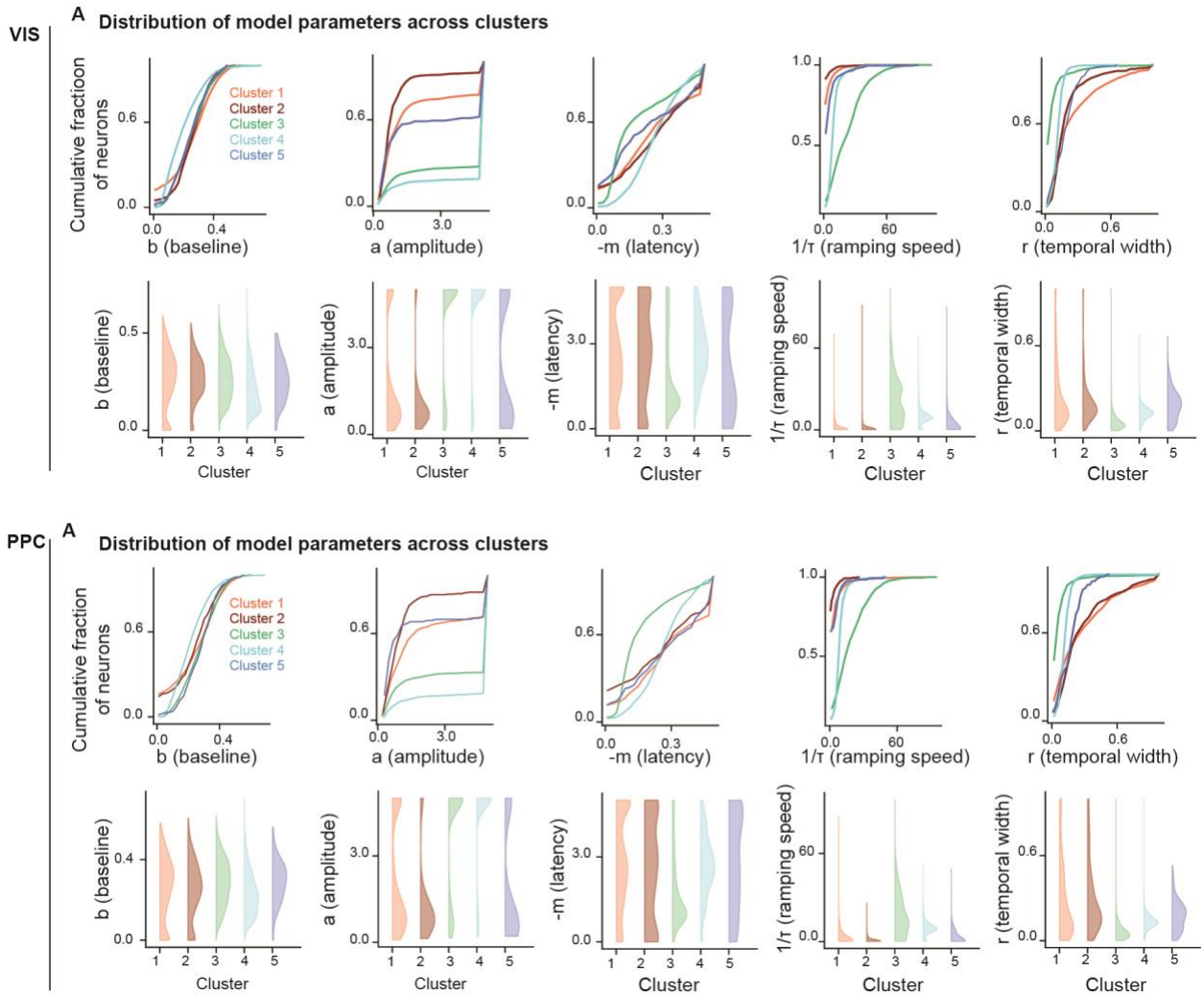

Supplemental Figure 3 (related to Fig. 6). Comparison of the 5 parameters of the temporal-receptive-field (TRF) model across all clusters (Orange, red: ramp-up clusters; Green, cyan, blue: ramp-down clusters). **Top:** cumulative histograms. **Bottom:** distributions.

'b' reflects the baseline shift and is similar across clusters since the activity is normalized.
'a' reflects the model response magnitude, which is bounded and clipped to avoid extreme values.
'm' reflects the time latency of activity peak, relative to stimulus onset.
'τ' is the time constant, reflecting the inverse of ramping speed.
'r' reflects the temporal width of the response.

Supplemental Figure 4

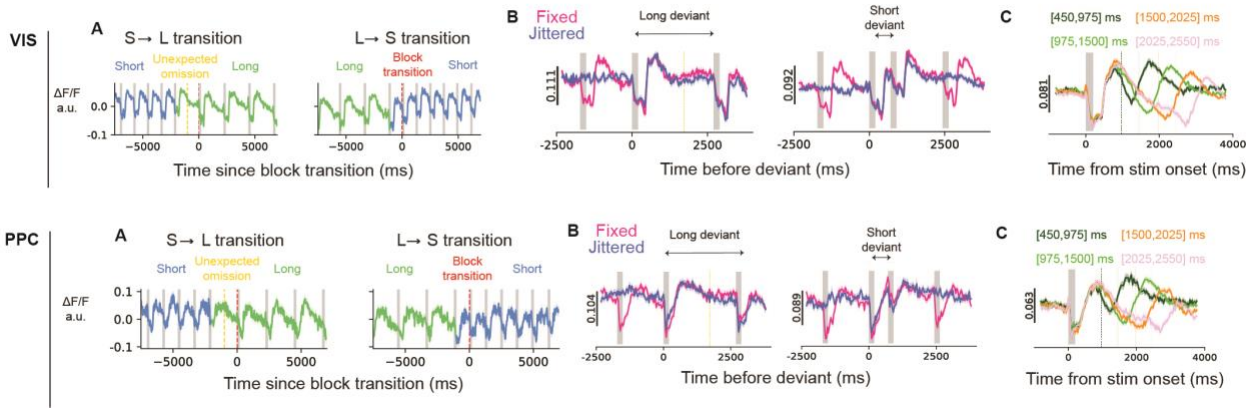

Supplemental Figure 4 (related to Figures 2-5). Response properties of neurons excluded from the TRF model. Excluded neurons showed response dynamics comparable to included neurons across all three paradigms. **VIS:** top panels; **PPC:** bottom panels**.**

A) Data from the short/long sessions. Trial-by-trial neural activity around block transitions. Similar to **Fig. 3 E**.

B) Neural responses (mean ± SEM) for each cluster, for fixed (red) and jittered (blue) blocks, aligned on the stimulus before the deviant ISI (**Left:** long deviant ISI; **Right:** short deviant ISI). Similar to **Fig. 4 A,E**.

C) Random ISIs divided into four bins (different colors). Neural responses averaged across trials within each ISI bin. Similar to **Fig. 5 F**.

Supplemental Figure 5

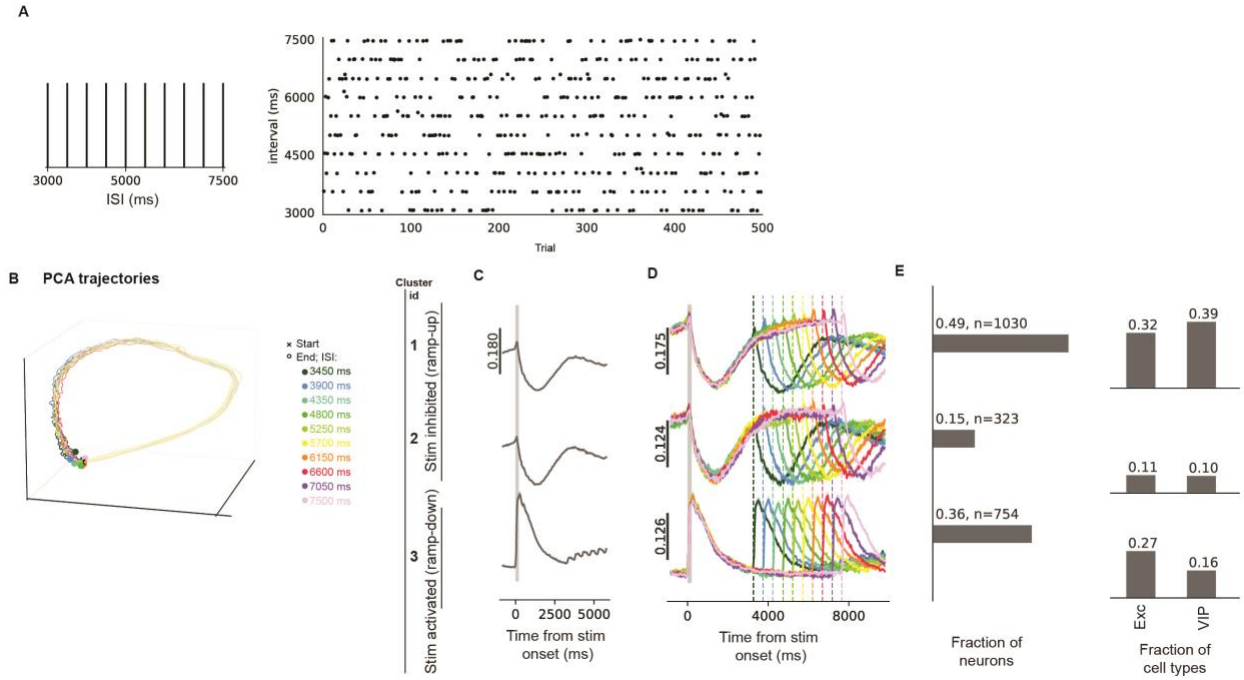

Supplemental Figure 5 (related to Fig. 5). Ramp-up neural responses plateau about 4s after stimulus onset. Data from extended-ISI random sessions (area VIS, 3 VIP-tdTomato mice, 5 sessions per mouse).

A) The extended random session is similar to the random session in **Fig. 1H** and **Fig. 5**, but with discrete, uniformly distributed ISIs in the range 3.0–7.5 s. **Left:** distribution of ISIs. **Right:** example sequence of consecutive trial ISIs.

B) Principal component analysis (top three components) of population activity from stimulus onset through the ISI. Trajectories follow a common manifold across intervals, extending further with longer ISIs.

C) Neuron- and trial-averaged responses aligned on the stimulus (gray box) for each cluster.

D) Neural responses averaged across trials within each ISI (different colors). Gray box: stimulus; vertical lines: ISIs.

C) Left: fraction of all neurons assigned to each cluster. **Right:** fraction of neurons of each cell type assigned to each cluster.

Supplemental Figure 6

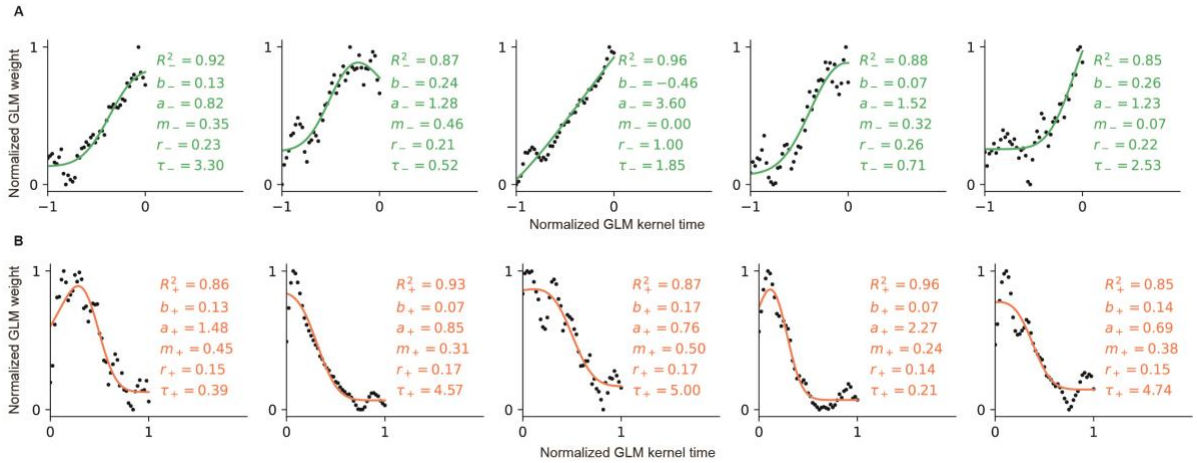

Supplemental Figure 6 (related to Figures 1-6). Example fits of GLM kernels using the TRF model.

A) Five examples of GLM kernel components fit by the ramp-up model. Goodness-of-fit values and model parameters are indicated. Dots: normalized GLM kernel weights before time 0. Green: ramp-up TRF model fit.

B) Same as (A), but for components fit by the ramp-down model. Orange: ramp-down TRF model fit.

References

Abbas, A. I., Sundiang, M. J. M., Henoch, B., Morton, M. P., Bolkan, S. S., Park, A. J., Harris, A. Z., Kellendonk, C., & Gordon, J. A. (2018). Somatostatin Interneurons Facilitate Hippocampal-Prefrontal Synchrony and Prefrontal Spatial Encoding. *Neuron*, *100*(4), 926-939.e923. https://doi.org/10.1016/j.neuron.2018.09.029

Abbott, L. F., & Regehr, W. G. (2004). Synaptic computation. *Nature*, *431*(7010), 796-803. https://doi.org/10.1038/nature03010

Abs, E., Poorthuis, R. B., Apelblat, D., Muhammad, K., Pardi, M. B., Enke, L., Kushinsky, D., Pu, D.-L., Eizinger, M. F., Conzelmann, K.-K., Spiegel, I., & Letzkus, J. J. (2018). Learning-Related Plasticity in Dendrite-Targeting Layer 1 Interneurons. *Neuron*, *100*(3), 684-699.e686. https://doi.org/https://doi.org/10.1016/j.neuron.2018.09.001

Adler, A., Zhao, R., Shin, M. E., Yasuda, R., & Gan, W. B. (2019). Somatostatin-Expressing Interneurons Enable and Maintain Learning-Dependent Sequential Activation of Pyramidal Neurons. *Neuron*, *102*(1), 202-216.e207. https://doi.org/10.1016/j.neuron.2019.01.036

Affan, R. O., Bright, I. M., Pemberton, L. N., Cruzado, N. A., Scott, B. B., & Howard, M. W. (2025). Ramping dynamics in the frontal cortex unfold over multiple timescales during motor planning. *Journal of Neurophysiology*, *133*(2), 625-637. https://doi.org/10.1152/jn.00234.2024

Aizenbud, I., Audette, N., Auksztulewicz, R., Basiński, K., Bastos, A. M., Berry, M., Canales-Johnson, A., Choi, H., Clopath, C., Cohen, U., Ponte Costa, R., De Filippo, R., Doronin, R., Errington, S. P., Gavornik, J. P., Gillon, C. J., Granier, A., Hamm, J. P., Hertäg, L.,...Sophy Xiong, Y. (2025). Neural mechanisms of predictive processing: a collaborative community experiment through the OpenScope program. arXiv:2504.09614. Retrieved April 01, 2025, from https://ui.adsabs.harvard.edu/abs/2025arXiv250409614A

Avanzini, P., Abdollahi, R. O., Sartori, I., Caruana, F., Pelliccia, V., Casaceli, G., Mai, R., Lo Russo, G., Rizzolatti, G., & Orban, G. A. (2016). Four-dimensional maps of the human somatosensory system. *Proc Natl Acad Sci U S A*, *113*(13), E1936-1943. https://doi.org/10.1073/pnas.1601889113

Barri, A., Wiechert, M. T., Jazayeri, M., & DiGregorio, D. A. (2022). Synaptic basis of a sub-second representation of time in a neural circuit model. *Nat Commun*, *13*(1), 7902. https://doi.org/10.1038/s41467-022-35395-y

Bastos, G., Holmes, J. T., Ross, J. M., Rader, A. M., Gallimore, C. G., Peterka, D. S., & Hamm, J. P. (2023). A frontosensory circuit for visual context processing is synchronous in the theta/alpha band. *bioRxiv*, 2023.2002.2025.530044. https://doi.org/10.1101/2023.02.25.530044

Bastos, G., Holmes, J. T., Ross, J. M., Rader, A. M., Gallimore, C. G., Wargo, J. A., Peterka, D. S., & Hamm, J. P. (2023). Top-down input modulates visual context processing through an interneuron-specific circuit. *Cell Rep*, *42*(9), 113133. https://doi.org/10.1016/j.celrep.2023.113133

Beierlein, M., Gibson, J. R., & Connors, B. W. (2003). Two dynamically distinct inhibitory networks in layer 4 of the neocortex. *Journal of Neurophysiology*, *90*(5), 2987-3000.

Benda, J., & Herz, A. V. (2003). A universal model for spike-frequency adaptation. *Neural Computation*, *15*(11), 2523-2564.

Bernacchia, A., Seo, H., Lee, D., & Wang, X. J. (2011). A reservoir of time constants for memory traces in cortical neurons. *Nat Neurosci*, *14*(3), 366-372. https://doi.org/10.1038/nn.2752

Boven, E., Pickford, J., Apps, R., & Cerminara, N. L. (2025). Cerebellar involvement in self-timing. *bioRxiv*, 2025.2003.2005.641568. https://doi.org/10.1101/2025.03.05.641568

Breska, A., & Deouell, L. Y. (2017). Neural mechanisms of rhythm-based temporal prediction: Delta phase-locking reflects temporal predictability but not rhythmic entrainment. *PLOS Biology*, *15*(2), e2001665. https://doi.org/10.1371/journal.pbio.2001665

Bueti, D., & Walsh, V. (2009). The parietal cortex and the representation of time, space, number and other magnitudes. *Philos Trans R Soc Lond B Biol Sci*, *364*(1525), 1831-1840. https://doi.org/10.1098/rstb.2009.0028

Buonomano, D. V., & Maass, W. (2009). State-dependent computations: spatiotemporal processing in cortical networks. *Nat Rev Neurosci*, *10*(2), 113-125. https://doi.org/10.1038/nrn2558

Cao, R., Bright, I. M., & Howard, M. W. (2024). Ramping cells in the rodent medial prefrontal cortex encode time to past and future events via real Laplace transform. *Proceedings of the National Academy of Sciences*, *121*(38), e2404169121. https://doi.org/doi:10.1073/pnas.2404169121

Carandini, M., & Heeger, D. J. (2012). Normalization as a canonical neural computation. *Nature Reviews Neuroscience*, *13*(1), 51-62.

Chabrol, F. P., Arenz, A., Wiechert, M. T., Margrie, T. W., & DiGregorio, D. A. (2015). Synaptic diversity enables temporal coding of coincident multisensory inputs in single neurons. *Nat Neurosci*, *18*(5), 718-727. https://doi.org/10.1038/nn.3974

Chubykin, A. A., Roach, E. B., Bear, M. F., & Shuler, M. G. (2013). A cholinergic mechanism for reward timing within primary visual cortex. *Neuron*, *77*(4), 723-735. https://doi.org/10.1016/j.neuron.2012.12.039

Churchland, M. M., Yu, B. M., Cunningham, J. P., Sugrue, L. P., Cohen, M. R., Corrado, G. S., Newsome, W. T., Clark, A. M., Hosseini, P., Scott, B. B., Bradley, D. C., Smith, M. A., Kohn, A., Movshon, J. A., Armstrong, K. M., Moore, T., Chang, S. W., Snyder, L. H., Lisberger, S. G.,...Shenoy, K. V. (2010). Stimulus onset quenches neural variability: a widespread cortical phenomenon. *Nature neuroscience*, *13*(3), 369-378. https://doi.org/10.1038/nn.2501

Cole, N., Harvey, M., Myers-Joseph, D., Gilra, A., & Khan, A. G. (2024). Prediction-error signals in anterior cingulate cortex drive task-switching. *Nature Communications*, *15*(1), 7088. https://doi.org/10.1038/s41467-024-51368-9

Coull, J. T., Cheng, R.-K., & Meck, W. H. (2011). Neuroanatomical and Neurochemical Substrates of Timing. *Neuropsychopharmacology*, *36*(1), 3-25. https://doi.org/10.1038/npp.2010.113

Cueva, C. J., Saez, A., Marcos, E., Genovesio, A., Jazayeri, M., Romo, R., Salzman, C. D., Shadlen, M. N., & Fusi, S. (2020). Low-dimensional dynamics for working memory and time encoding. *Proceedings of the National Academy of Sciences*, *117*(37), 23021-23032. https://doi.org/doi:10.1073/pnas.1915984117

De Corte, B. J., Akdoğan, B., & Balsam, P. D. (2022). Temporal scaling and computing time in neural circuits: Should we stop watching the clock and look for its gears? [Hypothesis and Theory]. *Frontiers in Behavioral Neuroscience*, *Volume 16 - 2022*. https://doi.org/10.3389/fnbeh.2022.1022713

de Vries, S. E. J., Lecoq, J. A., Buice, M. A., Groblewski, P. A., Ocker, G. K., Oliver, M., Feng, D., Cain, N., Ledochowitsch, P., Millman, D., Roll, K., Garrett, M., Keenan, T., Kuan, L., Mihalas, S., Olsen, S., Thompson, C., Wakeman, W., Waters, J.,...Koch, C. (2020). A large-scale standardized physiological survey reveals functional organization of the mouse visual cortex. *Nat Neurosci*, *23*(1), 138-151. https://doi.org/10.1038/s41593-019-0550-9

Feldman, D. E. (2012). The spike-timing dependence of plasticity. *Neuron*, *75*(4), 556-571. https://doi.org/10.1016/j.neuron.2012.08.001

Fiser, A., Mahringer, D., Oyibo, H. K., Petersen, A. V., Leinweber, M., & Keller, G. B. (2016). Experience-dependent spatial expectations in mouse visual cortex. *Nat Neurosci*, *19*(12), 1658-1664. https://doi.org/10.1038/nn.4385

Friston, K., & Kiebel, S. (2009). Predictive coding under the free-energy principle. *Philos Trans R Soc Lond B Biol Sci*, *364*(1521), 1211-1221. https://doi.org/10.1098/rstb.2008.0300

Fu, Y., Kaneko, M., Tang, Y., Alvarez-Buylla, A., & Stryker, M. P. (2015). A cortical disinhibitory circuit for enhancing adult plasticity. *Elife*, *4*, e05558. https://doi.org/10.7554/eLife.05558

Furutachi, S., Franklin, A. D., Aldea, A. M., Mrsic-Flogel, T. D., & Hofer, S. B. (2024). Cooperative thalamocortical circuit mechanism for sensory prediction errors. *Nature*, *633*(8029), 398-406. https://doi.org/10.1038/s41586-024-07851-w

Gao, Z., Davis, C., Thomas, A. M., Economo, M. N., Abrego, A. M., Svoboda, K., De Zeeuw, C. I., & Li, N. (2018). A cortico-cerebellar loop for motor planning. *Nature*, *563*(7729), 113-116. https://doi.org/10.1038/s41586-018-0633-x

Garcia-Garcia, M. G., Kapoor, A., Akinwale, O., Takemaru, L., Kim, T. H., Paton, C., Litwin-Kumar, A., Schnitzer, M. J., Luo, L., & Wagner, M. J. (2024). A cerebellar granule cell-climbing fiber computation to learn to track long time intervals. *Neuron*, *112*(16), 2749-2764.e2747. https://doi.org/10.1016/j.neuron.2024.05.019

Garrett, M., Groblewski, P., Piet, A., Ollerenshaw, D., Najafi, F., Yavorska, I., Amster, A., Bennett, C., Buice, M., Caldejon, S., Casal, L., D'Orazi, F., Daniel, S., Vries, S. E. d., Kapner, D., Kiggins, J., Lecoq, J., Ledochowitsch, P., Manavi, S.,...Olsen, S. R. (2023). Stimulus novelty uncovers coding diversity in visual cortical circuits. *bioRxiv*, 2023.2002.2014.528085. https://doi.org/10.1101/2023.02.14.528085

Garrett, M., Groblewski, P., Piet, A., Ollerenshaw, D., Yavorska, I., Najafi, F., Amster, A., Bennett, C., Buice, M., Caldejon, S., Casal, L., D'Orazi, F., Daniel, S., de Vries, S. E., Kapner, D., Kiggins, J., Lecoq, J., Ledochowitsch, P., Manavi, S.,...Olsen, S. R. (2023).

Stimulus novelty uncovers coding diversity in visual cortical circuits. *bioRxiv*, 2023.2002.2014.528085. https://doi.org/10.1101/2023.02.14.528085

Garrett, M., Manavi, S., Roll, K., Ollerenshaw, D. R., Groblewski, P. A., Ponvert, N. D., Kiggins, J. T., Casal, L., Mace, K., Williford, A., Leon, A., Jia, X., Ledochowitsch, P., Buice, M. A., Wakeman, W., Mihalas, S., & Olsen, S. R. (2020). Experience shapes activity dynamics and stimulus coding of VIP inhibitory cells. *Elife*, *9*. https://doi.org/10.7554/eLife.50340

Gavornik, J. P., & Bear, M. F. (2014). Learned spatiotemporal sequence recognition and prediction in primary visual cortex. *Nat Neurosci*, *17*(5), 732-737. https://doi.org/10.1038/nn.3683

Giovannucci, A., Badura, A., Deverett, B., Najafi, F., Pereira, T. D., Gao, Z., Ozden, I., Kloth, A. D., Pnevmatikakis, E., Paninski, L., De Zeeuw, C. I., Medina, J. F., & Wang, S. S. (2017). Cerebellar granule cells acquire a widespread predictive feedback signal during motor learning. *Nat Neurosci*, *20*(5), 727-734. https://doi.org/10.1038/nn.4531

Green, J., Bruno, C. A., Traunmüller, L., Ding, J., Hrvatin, S., Wilson, D. E., Khodadad, T., Samuels, J., Greenberg, M. E., & Harvey, C. D. (2023). A cell-type-specific error-correction signal in the posterior parietal cortex. *Nature*, *620*(7973), 366-373. https://doi.org/10.1038/s41586-023-06357-1

Hamm, J. P., Shymkiv, Y., Han, S., Yang, W., & Yuste, R. (2021). Cortical ensembles selective for context. *Proc Natl Acad Sci U S A*, *118*(14). https://doi.org/10.1073/pnas.2026179118

Harris, K. D., & Shepherd, G. M. G. (2015). The neocortical circuit: themes and variations. *Nature neuroscience*, *18*(2), 170-181. https://doi.org/10.1038/nn.3917

Hayashi, M. J., Ditye, T., Harada, T., Hashiguchi, M., Sadato, N., Carlson, S., Walsh, V., & Kanai, R. (2015). Time Adaptation Shows Duration Selectivity in the Human Parietal Cortex. *PLoS Biol*, *13*(9), e1002262. https://doi.org/10.1371/journal.pbio.1002262

Hennequin, G., Ahmadian, Y., Rubin, D. B., Lengyel, M., & Miller, K. D. (2018). The Dynamical Regime of Sensory Cortex: Stable Dynamics around a Single Stimulus-Tuned Attractor Account for Patterns of Noise Variability. *Neuron*, *98*(4), 846-860.e845. https://doi.org/https://doi.org/10.1016/j.neuron.2018.04.017

Hertäg, L., & Sprekeler, H. (2020). Learning prediction error neurons in a canonical interneuron circuit. *Elife*, *9*, e57541. https://doi.org/10.7554/eLife.57541

Herzfeld, D. J., & Lisberger, S. G. (2025). Neural circuit mechanisms to transform cerebellar population dynamics for motor control in monkeys. *bioRxiv*. https://doi.org/10.1101/2025.02.21.639459

Hockley, A., Bohórquez, L. H., & Malmierca, M. S. (2025). Top-down prediction signals from the medial prefrontal cortex govern auditory cortex prediction errors. *Cell Rep*, *44*(4), 115538. https://doi.org/10.1016/j.celrep.2025.115538

Hodgkin, A. L., & Huxley, A. F. (1952). A quantitative description of membrane current and its application to conduction and excitation in nerve. *J Physiol*, *117*(4), 500-544. https://doi.org/10.1113/jphysiol.1952.sp004764

Ibrahim, L. A., Huang, S., Fernandez-Otero, M., Sherer, M., Qiu, Y., Vemuri, S., Xu, Q., Machold, R., Pouchelon, G., Rudy, B., & Fishell, G. (2021). Bottom-up inputs are

required for establishment of top-down connectivity onto cortical layer 1 neurogliaform cells. *Neuron*, *109*(21), 3473-3485.e3475. https://doi.org/https://doi.org/10.1016/j.neuron.2021.08.004

Inagaki, H. K., Fontolan, L., Romani, S., & Svoboda, K. (2019). Discrete attractor dynamics underlies persistent activity in the frontal cortex. *Nature*, *566*(7743), 212-217. https://doi.org/10.1038/s41586-019-0919-7

Janssen, P., & Shadlen, M. N. (2005). A representation of the hazard rate of elapsed time in macaque area LIP. *Nat Neurosci*, *8*(2), 234-241. https://doi.org/10.1038/nn1386

Jaramillo, S., & Zador, A. M. (2011). The auditory cortex mediates the perceptual effects of acoustic temporal expectation. *Nat Neurosci*, *14*(2), 246-251. https://doi.org/10.1038/nn.2688

Jordan, R., & Keller, G. B. (2020). Opposing influence of top-down and bottom-up input on different types of excitatory layer 2/3 neurons in mouse visual cortex. *bioRxiv*.

Juavinett, A. L., Nauhaus, I., Garrett, M. E., Zhuang, J., & Callaway, E. M. (2017). Automated identification of mouse visual areas with intrinsic signal imaging. *Nature Protocols*, *12*(1), 32-43. https://doi.org/10.1038/nprot.2016.158

Kameda, M., Ohmae, S., & Tanaka, M. (2019). Entrained neuronal activity to periodic visual stimuli in the primate striatum compared with the cerebellum. *Elife*, *8*, e48702. https://doi.org/10.7554/eLife.48702

Keller, A. J., Roth, M. M., & Scanziani, M. (2020). Feedback generates a second receptive field in neurons of the visual cortex. *Nature*, *582*(7813), 545-549. https://doi.org/10.1038/s41586-020-2319-4

Keller, G. B., & Mrsic-Flogel, T. D. (2018). Predictive Processing: A Canonical Cortical Computation. *Neuron*, *100*(2), 424-435. https://doi.org/10.1016/j.neuron.2018.10.003

Kim, J., Ghim, J.-W., Lee, J. H., & Jung, M. W. (2013). Neural Correlates of Interval Timing in Rodent Prefrontal Cortex. *The Journal of Neuroscience*, *33*(34), 13834-13847. https://doi.org/10.1523/jneurosci.1443-13.2013

Knudstrup, S. G., Martinez, C., & Gavornik, J. P. (2025). Learned response dynamics reflect stimulus timing and encode temporal expectation violations in superficial layers of mouse V1. In: eLife Sciences Publications, Ltd.

Laje, R., & Buonomano, D. V. (2013). Robust timing and motor patterns by taming chaos in recurrent neural networks. *Nat Neurosci*, *16*(7), 925-933. https://doi.org/10.1038/nn.3405

Leon, M. I., & Shadlen, M. N. (2003). Representation of time by neurons in the posterior parietal cortex of the macaque. *Neuron*, *38*(2), 317-327. https://doi.org/10.1016/s0896-6273(03)00185-5

MacDonald, C. J., Lepage, K. Q., Eden, U. T., & Eichenbaum, H. (2011). Hippocampal "time cells" bridge the gap in memory for discontiguous events. *Neuron*, *71*(4), 737-749. https://doi.org/10.1016/j.neuron.2011.07.012

Machens, C. K., Romo, R., & Brody, C. D. (2010). Functional, But Not Anatomical, Separation of “What” and “When” in Prefrontal Cortex. *The Journal of Neuroscience*, *30*(1), 350-360. https://doi.org/10.1523/jneurosci.3276-09.2010

Mante, V., Sussillo, D., Shenoy, K. V., & Newsome, W. T. (2013). Context-dependent computation by recurrent dynamics in prefrontal cortex. *Nature*, *503*(7474), 78-84. https://doi.org/10.1038/nature12742

Marder, E., & Goaillard, J. M. (2006). Variability, compensation and homeostasis in neuron and network function. *Nat Rev Neurosci*, *7*(7), 563-574. https://doi.org/10.1038/nrn1949

Maristany de las Casas, E., Killmann, K., Drüke, M., Münster, L., Ebner, C., Sachdev, R., Jaeger, D., & Larkum, M. E. (2025). Tuft dendrites in frontal motor cortex enable flexible learning. *bioRxiv*, 2025.2003.2013.642781. https://doi.org/10.1101/2025.03.13.642781

Marshel, James H., Garrett, Marina E., Nauhaus, I., & Callaway, Edward M. (2011). Functional Specialization of Seven Mouse Visual Cortical Areas. *Neuron*, *72*(6), 1040-1054. https://doi.org/https://doi.org/10.1016/j.neuron.2011.12.004

Masland, R. H., & Martin, P. R. (2007). The unsolved mystery of vision. *Current Biology*, *17*(15), R577-R582. https://doi.org/https://doi.org/10.1016/j.cub.2007.05.040

Matell, M. S., Meck, W. H., & Nicolelis, M. A. (2003). Interval timing and the encoding of signal duration by ensembles of cortical and striatal neurons. *Behav Neurosci*, *117*(4), 760-773. https://doi.org/10.1037/0735-7044.117.4.760

Mauk, M. D., & Buonomano, D. V. (2004). The neural basis of temporal processing. *Annu Rev Neurosci*, *27*, 307-340. https://doi.org/10.1146/annurev.neuro.27.070203.144247

Medina, J. F., & Mauk, M. D. (2000). Computer simulation of cerebellar information processing. *Nat Neurosci*, *3 Suppl*, 1205-1211. https://doi.org/10.1038/81486

Mello, G. B., Soares, S., & Paton, J. J. (2015). A scalable population code for time in the striatum. *Curr Biol*, *25*(9), 1113-1122. https://doi.org/10.1016/j.cub.2015.02.036

Millman, D. J., Ocker, G. K., Caldejon, S., Kato, I., Larkin, J. D., Lee, E. K., Luviano, J., Nayan, C., Nguyen, T. V., North, K., Seid, S., White, C., Lecoq, J., Reid, C., Buice, M. A., & de Vries, S. E. J. (2020). VIP interneurons in mouse primary visual cortex selectively enhance responses to weak but specific stimuli. *Elife*, *9*, e55130. https://doi.org/10.7554/eLife.55130

Moberget, T., Karns, C. M., Deouell, L. Y., Lindgren, M., Knight, R. T., & Ivry, R. B. (2008). Detecting violations of sensory expectancies following cerebellar degeneration: a mismatch negativity study. *Neuropsychologia*, *46*(10), 2569-2579. https://doi.org/10.1016/j.neuropsychologia.2008.03.016

Murray, J. D., Bernacchia, A., Freedman, D. J., Romo, R., Wallis, J. D., Cai, X., Padoa-Schioppa, C., Pasternak, T., Seo, H., Lee, D., & Wang, X.-J. (2014). A hierarchy of intrinsic timescales across primate cortex. *Nature neuroscience*, *17*(12), 1661-1663. https://doi.org/10.1038/nn.3862

Najafi, F., Elsayed, G. F., Cao, R., Pnevmatikakis, E., Latham, P. E., Cunningham, J. P., & Churchland, A. K. (2020). Excitatory and Inhibitory Subnetworks Are Equally Selective during Decision-Making and Emerge Simultaneously during Learning. *Neuron*, *105*(1), 165-179 e168. https://doi.org/10.1016/j.neuron.2019.09.045

Najafi, F., Giovannucci, A., Wang, S. S., & Medina, J. F. (2014). Sensory-driven enhancement of calcium signals in individual Purkinje cell dendrites of awake mice. *Cell Rep*, *6*(5), 792-798. https://doi.org/10.1016/j.celrep.2014.02.001

Najafi, F., & Medina, J. F. (2013). Beyond "all-or-nothing" climbing fibers: graded representation of teaching signals in Purkinje cells. *Front Neural Circuits*, *7*, 115. https://doi.org/10.3389/fncir.2013.00115

Najafi, F., Russo, S., & Lecoq, J. (2025). Unexpected events trigger task-independent signaling in VIP and excitatory neurons of mouse visual cortex. *iScience*, *28*(2), 111728. https://doi.org/10.1016/j.isci.2024.111728

Narayanan, N. S. (2016). Ramping activity is a cortical mechanism of temporal control of action. *Curr Opin Behav Sci*, *8*, 226-230. https://doi.org/10.1016/j.cobeha.2016.02.017

Nitzan, N., & Buzsáki, G. (2025). Diversity of omission responses to visual images across brain-wide regions. *Sci Adv*, *11*(21), eadv5651. https://doi.org/10.1126/sciadv.adv5651

Nobre, A. C., Correa, A., & Coull, J. T. (2007). The hazards of time. *Current Opinion in Neurobiology*, *17*(4), 465-470.

O'Reilly, J. X., Mesulam, M. M., & Nobre, A. C. (2008). The cerebellum predicts the timing of perceptual events. *J Neurosci*, *28*(9), 2252-2260. https://doi.org/10.1523/jneurosci.2742-07.2008

Ohmae, S., Kunimatsu, J., & Tanaka, M. (2017). Cerebellar Roles in Self-Timing for Sub- and Supra-Second Intervals. *J Neurosci*, *37*(13), 3511-3522. https://doi.org/10.1523/jneurosci.2221-16.2017

Pachitariu, M., Stringer, C., Dipoppa, M., Schröder, S., Rossi, L. F., Dalgleish, H., Carandini, M., & Harris, K. D. (2017). Suite2p: beyond 10,000 neurons with standard two-photon microscopy. *bioRxiv*, 061507. https://doi.org/10.1101/061507

Pastalkova, E., Itskov, V., Amarasingham, A., & Buzsáki, G. (2008). Internally generated cell assembly sequences in the rat hippocampus. *Science*, *321*(5894), 1322-1327. https://doi.org/10.1126/science.1159775

Paton, J. J., & Buonomano, D. V. (2018). The Neural Basis of Timing: Distributed Mechanisms for Diverse Functions. *Neuron*, *98*(4), 687-705. https://doi.org/10.1016/j.neuron.2018.03.045

Pi, H.-J., Hangya, B., Kvitsiani, D., Sanders, J. I., Huang, Z. J., & Kepecs, A. (2013). Cortical interneurons that specialize in disinhibitory control. *Nature*, *503*(7477), 521-524. https://doi.org/10.1038/nature12676

Piscopo, D. M., El-Danaf, R. N., Huberman, A. D., & Niell, C. M. (2013). Diverse Visual Features Encoded in Mouse Lateral Geniculate Nucleus. *The Journal of Neuroscience*, *33*(11), 4642-4656. https://doi.org/10.1523/jneurosci.5187-12.2013

Price, B. H., Jensen, C. M., Khoudary, A. A., & Gavornik, J. P. (2023). Expectation violations produce error signals in mouse V1. *Cerebral Cortex*, *33*(13), 8803-8820. https://doi.org/10.1093/cercor/bhad163

Rajan, K., Abbott, L. F., & Sompolinsky, H. (2010). Stimulus-dependent suppression of chaos in recurrent neural networks. *Physical Review E*, *82*(1), 011903. https://doi.org/10.1103/PhysRevE.82.011903

Rao, R. P., & Ballard, D. H. (1999). Predictive coding in the visual cortex: a functional interpretation of some extra-classical receptive-field effects. *Nat Neurosci*, *2*(1), 79-87. https://doi.org/10.1038/4580

Rodieck, R. W. (1967). Maintained activity of cat retinal ganglion cells. *J Neurophysiol*, *30*(5), 1043-1071. https://doi.org/10.1152/jn.1967.30.5.1043

Sara, S. J., & Bouret, S. (2012). Orienting and reorienting: the locus coeruleus mediates cognition through arousal. *Neuron*, *76*(1), 130-141. https://doi.org/10.1016/j.neuron.2012.09.011

Schneider, B. A., & Ghose, G. M. (2012). Temporal production signals in parietal cortex. *PLoS Biol*, *10*(10), e1001413. https://doi.org/10.1371/journal.pbio.1001413

Schneider, D. M., Sundararajan, J., & Mooney, R. (2018). A cortical filter that learns to suppress the acoustic consequences of movement. *Nature*, *561*(7723), 391-395. https://doi.org/10.1038/s41586-018-0520-5

Seamans, J. K., & Yang, C. R. (2004). The principal features and mechanisms of dopamine modulation in the prefrontal cortex. *Prog Neurobiol*, *74*(1), 1-58. https://doi.org/10.1016/j.pneurobio.2004.05.006

Shadmehr, R., Smith, M. A., & Krakauer, J. W. (2010). Error correction, sensory prediction, and adaptation in motor control. *Annu Rev Neurosci*, *33*, 89-108. https://doi.org/10.1146/annurev-neuro-060909-153135

Shin, H., & Adesnik, H. (2021). NDNF interneurons, Spartans of the cortical column: Small in number, strong in impact. *Neuron*, *109*(13), 2041-2042. https://doi.org/https://doi.org/10.1016/j.neuron.2021.06.022

Shuler, M. G., & Bear, M. F. (2006). Reward timing in the primary visual cortex. *Science*, *311*(5767), 1606-1609. https://doi.org/10.1126/science.1123513

Steinmetz, N. A., Zatka-Haas, P., Carandini, M., & Harris, K. D. (2019). Distributed coding of choice, action and engagement across the mouse brain. *Nature*, *576*(7786), 266-273. https://doi.org/10.1038/s41586-019-1787-x

Stringer, C., & Pachitariu, M. (2025). Cellpose3: one-click image restoration for improved cellular segmentation. *Nature Methods*, *22*(3), 592-599. https://doi.org/10.1038/s41592-025-02595-5

Suvrathan, A., Payne, H. L., & Raymond, J. L. (2016). Timing Rules for Synaptic Plasticity Matched to Behavioral Function. *Neuron*, *92*(5), 959-967. https://doi.org/10.1016/j.neuron.2016.10.022

Szadai, Z., Pi, H. J., Chevy, Q., Ócsai, K., Albeanu, D. F., Chiovini, B., Szalay, G., Katona, G., Kepecs, A., & Rózsa, B. (2022). Cortex-wide response mode of VIP-expressing inhibitory neurons by reward and punishment. *Elife*, *11*. https://doi.org/10.7554/eLife.78815

Tesche, C. D., & Karhu, J. J. (2000). Anticipatory cerebellar responses during somatosensory omission in man. *Hum Brain Mapp*, *9*(3), 119-142.

The International Brain, L., Aguillon-Rodriguez, V., Angelaki, D., Bayer, H., Bonacchi, N., Carandini, M., Cazettes, F., Chapuis, G., Churchland, A. K., Dan, Y., Dewitt, E., Faulkner, M., Forrest, H., Haetzel, L., Häusser, M., Hofer, S. B., Hu, F., Khanal, A., Krasniak, C.,...Zador, A. M. (2021). Standardized and reproducible measurement of decision-making in mice. *Elife*, *10*, e63711. https://doi.org/10.7554/eLife.63711

Tremblay, R., Lee, S., & Rudy, B. (2016). GABAergic Interneurons in the Neocortex: From Cellular Properties to Circuits. *Neuron*, *91*(2), 260-292. https://doi.org/10.1016/j.neuron.2016.06.033

Tsao, A., Yousefzadeh, S. A., Meck, W. H., Moser, M. B., & Moser, E. I. (2022). The neural bases for timing of durations. *Nat Rev Neurosci*, *23*(11), 646-665. https://doi.org/10.1038/s41583-022-00623-3

Tsodyks, M. V., & Markram, H. (1997). The neural code between neocortical pyramidal neurons depends on neurotransmitter release probability. *Proceedings of the National Academy of Sciences*, *94*(2), 719-723.

Van Derveer, A. B., Ross, J. M., & Hamm, J. P. (2023). Robust multisensory deviance detection in the mouse parietal associative area. *Curr Biol*, *33*(18), 3969-3976.e3964. https://doi.org/10.1016/j.cub.2023.08.002

Vélez-Fort, M., Rousseau, C. V., Niedworok, C. J., Wickersham, I. R., Rancz, E. A., Brown, A. P., Strom, M., & Margrie, T. W. (2014). The stimulus selectivity and connectivity of layer six principal cells reveals cortical microcircuits underlying visual processing. *Neuron*, *83*(6), 1431-1443. https://doi.org/10.1016/j.neuron.2014.08.001

Wang, J., Narain, D., Hosseini, E. A., & Jazayeri, M. (2018). Flexible timing by temporal scaling of cortical responses. *Nature neuroscience*, *21*(1), 102-110. https://doi.org/10.1038/s41593-017-0028-6

Wang, S., Falcone, R., Richmond, B., & Averbeck, B. B. (2023). Attractor dynamics reflect decision confidence in macaque prefrontal cortex. *Nat Neurosci*, *26*(11), 1970-1980. https://doi.org/10.1038/s41593-023-01445-x

Wang, X.-J. (2008). Decision Making in Recurrent Neuronal Circuits. *Neuron*, *60*(2), 215-234. https://doi.org/10.1016/j.neuron.2008.09.034

Wang, X. J. (2008). Decision making in recurrent neuronal circuits. *Neuron*, *60*(2), 215-234. https://doi.org/10.1016/j.neuron.2008.09.034

Wei, Z., Lin, B.-J., Chen, T.-W., Daie, K., Svoboda, K., & Druckmann, S. (2020). A comparison of neuronal population dynamics measured with calcium imaging and electrophysiology. *PLOS Computational Biology*, *16*(9), e1008198. https://doi.org/10.1371/journal.pcbi.1008198

Xu, M., Zhang, S. Y., Dan, Y., & Poo, M. M. (2014). Representation of interval timing by temporally scalable firing patterns in rat prefrontal cortex. *Proc Natl Acad Sci U S A*, *111*(1), 480-485. https://doi.org/10.1073/pnas.1321314111

Yaron, A., Shiramatsu-Isoguchi, T., Kern, F. B., Ohki, K., Takahashi, H., & Chao, Z. C. (2024). Omission-responsive neurons encode negative prediction error and probability in the auditory cortex. *bioRxiv*, 2024.2009.2009.612166. https://doi.org/10.1101/2024.09.09.612166

Yu, Q., Bi, Z., Jiang, S., Yan, B., Chen, H., Wang, Y., Miao, Y., Li, K., Wei, Z., & Xie, Y. (2022). Visual cortex encodes timing information in humans and mice. *Neuron*, *110*(24), 4194-4211. e4110.

Zhang, Q., Grødem, S., Gracias, A., Lensjø, K. K., Fyhn, M., Stringer, C., & Pachitariu, M. (2025). Spatial predictive coding in visual cortical neurons. *bioRxiv*, 2025.2009.2017.676794. https://doi.org/10.1101/2025.09.17.676794

Zhang, Y., Rózsa, M., Liang, Y., Bushey, D., Wei, Z., Zheng, J., Reep, D., Broussard, G. J., Tsang, A., Tsegaye, G., Narayan, S., Obara, C. J., Lim, J.-X., Patel, R., Zhang, R., Ahrens, M. B., Turner, G. C., Wang, S. S. H., Korff, W. L.,...Looger, L. L. (2023). Fast and sensitive GCaMP calcium indicators for imaging neural populations. *Nature*, *615*(7954), 884-891. https://doi.org/10.1038/s41586-023-05828-9

Zhou, S., Masmanidis, S. C., & Buonomano, D. V. (2020). Neural Sequences as an Optimal Dynamical Regime for the Readout of Time. *Neuron*, *108*(4), 651-658.e655. https://doi.org/10.1016/j.neuron.2020.08.020

Zhou, Z. C., Huang, W. A., Yu, Y., Negahbani, E., Stitt, I. M., Alexander, M. L., Hamm, J. P., Kato, H. K., & Fröhlich, F. (2020). Stimulus-specific regulation of visual oddball differentiation in posterior parietal cortex. *Sci Rep*, *10*(1), 13973. https://doi.org/10.1038/s41598-020-70448-6

Zhuang, J., Ng, L., Williams, D., Valley, M., Li, Y., Garrett, M., & Waters, J. (2017). An extended retinotopic map of mouse cortex. *Elife*, *6*, e18372. https://doi.org/10.7554/eLife.18372

Zucker, R. S., & Regehr, W. G. (2002). Short-term synaptic plasticity. *Annu Rev Physiol*, *64*, 355-405. https://doi.org/10.1146/annurev.physiol.64.092501.114547